APPLICATION OF IMAGE BASED FINITE ELEMENT ANALYSIS FOR MECHANICAL CHARACTERIZATION OF MATERIALS PROCESSED BY DIRECT ENERGY DEPOSITION TECHNOLOGY

A Thesis
Submitted to the Graduate Faculty
of the
North Dakota State University
of Agriculture and Applied Science

By

David Jordan Smith

In Partial Fulfillment of the Requirements
for the Degree of
MASTER OF SCIENCE

Major Department:
Mechanical Engineering

April 2024

Fargo, North Dakota

North Dakota State University
Graduate School

Title

Application of Image Based Finite Element Analysis for Mechanical Characterization of Materials Processed by Direct Energy Deposition Technology

By

David Jordan Smith

The Supervisory Committee certifies that this ***thesis*** complies with North Dakota State University's regulations and meets the accepted standards for the degree of

MASTER OF SCIENCE

SUPERVISORY COMMITTEE:

Dr. Fardad Azarmi
Chair

Dr. Alan Kallmeyer

Dr. Annie Tangpong

Dr. Ying Huang

Approved:

4/12/2024	Dr. Chad Ulven
Date	Department Chair

ABSTRACT

The main focus of this study is to analyze the elastic properties of two different additively manufactured materials. To this end, a cobalt chromium (CoCr) metal alloy sample and a tungsten carbide-17% cobalt (WC-17Co) cermet specimen were both fabricated by the direct energy deposition (DED) process and were examined in this study. A comparative study between the results obtained from the application of numerical and analytical techniques versus the experimental results could show the accuracy of these techniques for estimation of elastic properties of the samples. A conventionally manufactured CoCr alloy and WC-17Co samples with similar composition was subjected to the same analysis for the purpose of validation of the results. The object oriented finite element analysis (OOF) technique provided acceptable results for the DED processed CoCr sample, but was unsuccessful in the estimation of the elastic behavior of WC-Co DED sample due to its inhomogeneous microstructure.

ACKNOWLEDGMENTS

I would like to thank my advisor Dr. Fardad Azarmi for giving me the opportunity to research under his supervision during my time at NDSU. His guidance and assistance were a great help and allowed me to progress throughout the program. I would also like to thank my committee members Dr. Alan Kallmeyer, Dr. Annie Tangpong, and Dr. Ying Huang for their time and consideration during the course of this project.

I would like to thank the U.S. Department of Defense, the Ground Vehicles Systems Center, and the National Center for Manufacturing Sciences for their investment in the project. Specifically, I would like to thank Martin McDonnell, Matthew Rogers, and Scott Benton for their assistance throughout my research.

I would like to thank Scott Payne and his assistance at the Microscopy Center at NDSU for his assistance in SEM/EDS of the samples used in this study, as well as Theresa Grabowski and Joncy Thorpe for their help in supplying some SEM and hardness testing results of the CoCr samples. Finally, I would like to thank the rest of my fellow research assistants for their help and support throughout my time in the master’s program at NDSU.

DEDICATION

I want to dedicate this research to my parents,

Gordy and Arvy Smith

Who always saw the best in me and pushed me to achieve it.

I could not have done this without your constant love and support.

And to my closest friends

Thank you for always believing in me.

TABLE OF CONTENTS

LIST OF TABLES

Table Page

LIST OF FIGURES

LIST OF ABBREVIATIONS

AM	Additive Manufacturing
BJT	Binder Jetting
CCAT	Connecticut Center of Advanced Technology
CoCr	Cobalt Chromium
DED	Direct Energy Deposition
DLF	Direct Light Fabrication
DMD	Direct Metal Deposition
DMT	Direct Metal Tooling
EBAM	Electron Beam Additive Manufacturing
EDM	Electric Discharge Machine
EDS	Energy Dispersive Spectroscopy
FEA	Finite Element Analysis
HVAF	High Velocity Air Fuel
HVOF	High Velocity Oxygen Fuel
LC	Laser Cladding
LENS	Laser Engineered Net Shaping
MEX	Material Extrusion
MJT	Material Jetting
NIST	National Institute of Standards and Technology
OM	Optical Microscopy
OOF	Object Oriented Finite Element Analysis
PBF	Powder Bed Fusion
RFDA	Resonance Frequency Data Analyzer
RoM	Rule of Mixture
SEM	Scanning Electron Microscopy
SHL	Sheet Lamination
SLM	Selective Laser Melting
VPP	Vat Photopolymerization
WC-Co	Tungsten Carbide Cobalt

LIST OF APPENDIX FIGURES

1. INTRODUCTION

Additive manufacturing (AM) has become an important part of manufacturing science and has successfully been applied in numerous industries. This process is also known as 3D printing and includes a wide range of advanced manufacturing technologies that allow complex geometries and designs to be fabricated with less waste and in fewer number of fabrication steps in comparison with most of the traditional manufacturing methods. In fact, fabrication of some parts and components with complicated geometries is not possible through conventional manufacturing methods and it only became possible after introduction of AM technology [1, 2]. While the concept of AM started with prototyping and manufacturing of polymeric and soft materials, further advancements in this technology have made metal and ceramic printing extremely popular within both research and industry sectors. Aerospace, automotive, electronics, biomedical, orthopedic, orthodontic, and custom tooling are among different industries actively implemented AM technology for manufacturing parts and components [3, 4].

Historically, AM was referred to as a solid freeform fabrication or additive layer manufacturing method and it is based on joining materials in a layer-by-layer style. This makes AM different from other fabrication techniques that involve forming or subtractive manufacturing. The heart of the process is direct fabrication of the parts from CAD models, which is possible by interfacing a computer and manufacturing device. In recent years, several different processes were introduced to the market with the capability of adding material in a layer-by-layer manner for near-net-shape formation of desired geometry [5]. ASTM 52900 standardized these different AM technologies to seven major categories. These are binder jetting (BJT), direct energy deposition (DED), material extrusion (MEX), material jetting (MJT), powder bed fusion (PBF), sheet lamination (SHL), and vat photopolymerization (VPP). These main categories can then be broken down further into subcategories such as selective laser melting (SLM), laser beam DED, and chemically bonded material jetting [6]. Rapid prototyping and fabrication of complex structures and functionally graded materials are among other capabilities of AM technologies in modern technologies [7, 8, 9].

Metal AM allows for a digital 3D model to come to life using different processes such as fusion of material layers or deposition of locally melted metallic particles on the printing stage [10]. It is an advanced technology that can be used either for fabrication of entire parts and components or to repair and rebuild selective regions of the damaged parts [11]. Some studies showed the dependency of the microstructure of AM processed metals and alloys to the operational process parameters [3]. Due to the high volume of different combinations of materials and additive manufacturing processes, there are numerous relationships between process parameters and mechanical properties. Recently, machine learning has been employed to optimize process parameters of AM technology for metal fabrication [12].

Direct energy deposition (DED) is a specific class of AM technologies that has recently found its place in the metal fabrication industry due to its unique characteristics and advantages [13]. In this process, thermal energy is consumed to fuse deposited powder materials in separate layers according to a 3D model generated by CAD software. Laser, electron beam, or plasma arc is utilized in this technology to melt feed stock powder materials on to the printing platform. To avoid excessive oxidation, the DED process will be performed in a controlled (inert) environment when thermal energy is provided from a laser or plasma source, while technologies employing electron beam systems usually operate in a vacuum condition [14]. There are different modes and types of DED processes as classified according to ASTM F3187-16 [15]. Laser engineered net shaping (LENS), direct metal deposition (DMD), 3D laser cladding (LC), direct light fabrication (DLF), and electron beam additive manufacturing (EBAM) are among different classes of DED processes [10].

Unlike some other manufacturing processes, DED allows powders to be mixed either before the beginning of the deposition or while the powders are enroute to the printing stage. This allows for deposition of graded materials and will make it possible for the material composition to change throughout a part or tool. This capability gives DED an important advantage over the other metal AM technologies because it provides the ability to have specific (desired) characteristics and properties at selected regions of a part. The heat input and powder in-flight velocity must be closely monitored and controlled by adjusting the power during the DED process [14]. Other process parameters such as feed rate, gas flow, and build speed are important operational parameters that can determine the properties of the DED processed parts. Generally, it is found that a smooth surface finish with finer grains can be obtained if the melt pool is small; however, it will drastically increase the deposition (printing) time. As it was mentioned before for AM technologies, the process parameters can also control mechanical properties such as the ultimate tensile strength, fatigue strength, hardness, yield strength, and toughness in DED processed samples [6, 15].

Specific applications such as dentures and implants require biocompatible materials that can function in corrosive and degrading environments such as living bodies and tissues. Advanced materials with unique biocompatibility are required to be used for applications such as joint replacements, orthopedic fixations, stents, or dental implants to avoid complications like infection, inflammation, pain, or loss of function in patients after surgery [8, 9, 16]. Titanium and its alloys, nickel free stainless steels, and cobalt chromium (CoCr) are among the most commonly used metallic biomaterials. Several recent studies have focused on CoCr alloys because of the high corrosion and wear resistance as well as its excellent strength and stiffness [17, 18]. Some other research works have been conducted to investigate the use of CoCr alloys in medical devices. These studies determined that CoCr and its alloys are well-suited materials for applications that require long-term corrosion and wear resistance because of the strain-induced martensitic transformation in its microstructure. The transformation from face-centered-cubic (FCC) to hexagonal-close-packed (HCP) structure has been shown to enhance the work hardening during plastic deformation, which increases wear resistance of CoCr alloys [19, 20]. This improved wear resistance is very beneficial for a variety of biomedical implants, prostheses, and aerospace applications [9].

Due to their high hardness, high wear resistance, and low thermal conductivity, machining conventionally processed parts and components made from CoCr alloys is a challenging task [22]. Therefore, AM that fabricates final products could be considered as a prime alternative to overcome those post-fabrication machining limitations [23]. Through significant development, 3D printing seems to be a promising method for producing highly detailed and complex parts that are suitable for custom medical implants. With the added benefit of CAD in AM, models for implants can be checked accurately and modified before production. The selection of optimum process parameters in AM technology makes it possible to obtain parts with desired properties and characteristics required for bio-applications [24]. In addition, parts fabricated from CoCr and its alloys via additive manufacturing exhibit anisotropic mechanical properties due to the fact that materials can be deposited, melted, fused, and solidified in different crystallographic directions [1, 2].

Available research studies on additively manufactured processed CoCr alloys mostly focused on some general microstructural and mechanical properties of the samples produced by selective laser melting (SLM) technology [11, 23]. Characteristics such as density, stiffness, strength, and corrosion resistance with respect to the desired geometry were investigated in SLM processed CoCr samples [26]. However, since DED is a relatively newer AM technology, only a few studies have been performed that focused on properties of DED processed CoCr samples. Sartika *et al*. studied the effect of insufficient laser energy on powder melting process, chemical inhomogeneity, and consequently improper fusion during DED process of CoCr based materials [27]. Unfortunately, there is a lack of research on the general mechanical properties of DED processed CoCr as well as specific mechanical characteristics which could be important for biocompatible devices and components.

Another commonly used industrial material that exhibits excellent mechanical properties for tribological applications is Tungsten carbide cobalt (WC-Co). This cermet material is one of the most widely used materials for wear-resistant parts, molds, mining parts, and cutting tools [28]. It possesses superior hardness, compressive strength, and fracture toughness, as well as high wear resistance and corrosion resistance. The WC-Co composite is a good mixture of hard carbide phase with a soft and ductile cobalt metal that increases flexibility of the components fabricated from this material [29].

Generally, fabrication of hard materials such as carbides and nitrides with high temperature resistance is a challenging task. In addition, molding methods must account for significant shrinkage and a limited ability to produce parts with complex shapes and geometries without the requirements of costly post process machining [28]. However, thermal spraying methods have been used to successfully deposit protective coatings from such hard materials on the surface of steel tools and parts to increase their surface properties including wear, hardness, and thermal resistance. Typically, in thermal spraying, fuels mixed with oxygen and air create a high temperature flame. Adding powders of alloys, ceramics, or cermets to this hot flame jet results in softening or melting of the particles. For spraying WC-Co particles, it is expected that Co particle are completely melted while WC is partially melted or softened [29].

The fabrication of parts and components made from WC-Co using traditional manufacturing methods could be a challenging task due to the requirements of taking several steps such as the molding, shaping, heat treatment, and machining processes. To this end, there is a huge interest in the utilization of AM technologies in fabrication of WC-Co parts. Technologies such as SLM and binder jet additive manufacturing (BJAM) are the most attempted to produce WC-Co parts, but they are still far from being perfect, and parts produced using these techniques contain flaws and deficiencies. These include inefficient mechanical properties due to defects such as cracks and porosities [28]. Most studies on using these methods to produce WC-Co using AM are focused on optimization of printing parameters and properties to reduce these flaws that hinder its further use. There have been fewer studies on WC-Co parts processed using DED compared to SLM and BJAM, but this method presents many potential benefits that could make it ideal. One unique advantage of DED technology is the ability to quickly and easily produce large parts without reusing powders as the BJAM and SLM technologies do [30]. Existing studies on WC-Co produces by DED focus on compositions of the cermet with 10-12% cobalt content, but to the author’s knowledge no prior studies have been conducted on samples with 17% cobalt content.

There are also existing challenges in accurate measurement of the mechanical properties of parts produced using these AM technologies. Specifically, the elastic properties of AM materials are particularly difficult to measure due to a variety of factors. Currently there is no reliable standard that can be used for accurate estimation of the tensile properties of AM produced parts. ASTM F3122 lists usable standards for measuring the tensile properties of an AM sample, but specifically notes that the results can be affected by many factors such as feedstock material, anisotropy, material and specimen preparation, porosity, testing environment, alignment, and testing parameters [31]. The standard also notes the geometrical difficulties in producing the tensile test samples using some AM technologies. The dog-bone sample is also not ideal for reproduceable tests of AM materials due to the curved fillets separating the clamp area and the cross-section of the sample [32]. These curved areas can lead to stress concentrations, nonlinear loading, gaps, and additional roughness along the fillets depending on the printing path. A diagram by Sola clearly explains these issues as depicted in Figure 1.

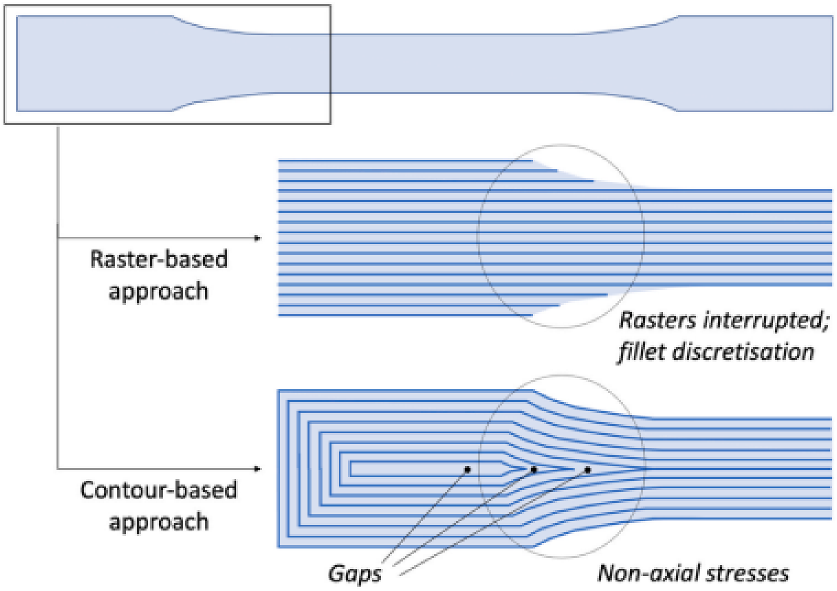

Figure 1. Examples of printing issues and resulting defects of AM dog-bone tensile samples [32].

Furthermore, accessibility of a tool that is able to accurately predict the elastic modulus of a sample without the need for mechanical testing would be very beneficial to the industry. Having the ability to simulate the tensile properties of different samples without any need for experimental examination may result in huge cost saving. Finite element analysis (FEA) has been used for simulating stress and other mechanical conditions for many years, but numerical simulations typically rely on the input of the material properties rather than solving for them. One emerging numerical simulation method that has the potential to accomplish this is object oriented finite element analysis (OOF). This finite element scheme developed by the National Institute of Standards and Technology (NIST) uses actual microstructural images and includes features such as porosities, multiple phases, or impurities in its simulations.

This study will utilize this novel finite element approach to predict the elastic properties of AM processed samples. Some well-known analytical methods for prediction of mechanical properties of materials will also be utilized to evaluate their capability for estimation of tensile properties of AM produced WC-Co materials in this study. The successful results from this study can provide access to a new tool to estimate important mechanical properties of AM processed materials independent of experimental tests.

2. OBJECTIVE

DED is a growing AM technology in recent years and there is a huge need for understanding of the mechanical properties of parts produced using this technology. DED processed CoCr alloy and WC-Co were selected to represent metallic and ceramic samples in this study. This study will focus on using various methods to approximate the elastic properties of DED processed samples, aiming to show the usefulness of models and simulations in estimating these properties independent from experimental mechanical testing. For reason of comparison, all tests and characterizations were also performed on conventionally processed samples in this study. The elastic modulus was then estimated on all samples using experimental, analytical, and numerical methods. These results were compared for the purpose of analyzing the benefits and drawbacks of each method when approximating the tensile properties of a nonhomogeneous DED produced material. Both CoCr and WC-Co samples studied here are among important industrial and commercially used materials with wide ranges of applications.

3. MATERIALS AND EXPERIMENTAL PROCEDURE

3.1 Materials and Sample Preparation

3.1.1 Direct Energy Deposition of CoCr

Direct Metal Tooling® (DMT®) by InssTek Inc., South Korea was used to fabricate the CoCr samples in this study. An SDM 800 Module was used to deposit layers during the DED process. This particular system operates using an Ytterbium laser system and it is equipped with two cameras that are used as sensors during the printing process. Shielding gas was used during the printing process to prevent the exposure of the printed samples to harmful gases such as oxygen and hydrogen. The thickness of the deposited layers is referred to as "layer height", and "powder feeding rate" is the speed at which the powder is fed into the deposition system. The printing parameters for the samples are shown in Table 1. The dimensions of the DED fabricated samples were 40 mm $(L)\times$ 5 mm (W) × 5 (H) mm.

Table 1. DED CoCr Printing Process Parameters.

Process Parameter	Value
Beam Size of Laser (μm)	800
Build Speed (cm^3/h)	33
Layer Height (μm)	250
Laser Power (W)	360
Powder Feeding Rate (g/min)	2.5
Coaxial Gas Feed Rate (L/min)	6.5
Powder Gas Feed Rate (L/min)	2.5
Shielding Gas	Argon

3.1.2 Conventionally Processed CoCr

The bar stock samples from Titanium Industries Inc., Rockaway, NJ, USA, fabricated by powder metallurgy were used as conventionally processed samples in this study. All bar stock samples were cut using an Electric Discharge Machine (EDM) into rectangles at 40 (L) × 5 (W) × 5 (H) mm sizes as well as disks with a diameter of 12.7 mm and a height of 5 mm.

3.1.3 Material Composition of CoCr

Table 2 lists the nominal composition of the DED and conventional samples that were provided by the manufacturers of both samples. Their chemical compositions are very close with the cobalt content being slightly (2%) higher in the conventional sample as well as having a 2% decrease in chromium content compared to the DED sample.

Table 2. Composition of CoCr Alloy Samples.

Element	Co	Cr	Mo	Ni	C
DED Nominal Composition from InssTek (wt.%)	64.78	29.16	5.18	-	0.88
Composition of Conventional Sample (wt.%)	66	27	5.5	0.2	0.05

3.1.4 Direct Energy Deposition of WC-Co

An Optomic 850R LENS AM machine at the Connecticut Center of Advanced Technology (CCAT), CT, USA was used to fabricate the AM WC-Co samples in this study. This system utilizes a 3 kW IPG fiber laser system and three separate powder feeders to deposit 2 mm wide passes of material. Other important printing parameters are listed in Table 3. The sample was developed on an H13 tool steel substrate with dimensions of 75 (L) × 75 (W) × 5 (H) mm. The DED deposited layer had a thickness of 800 μm. The samples were then cut using EDM for mechanical testing at the size of 40 × 5 × 5 mm.

Table 3. DED WC-Co Printing Parameters.

Process Parameter	Value
Powder Flow	5 L/min
Center Purge	35 L/min
Powder Flow Rate	4.5 rev/min
Laser Power	708 W
Laser Spot Size	2 mm
Contour Travel Write Speed	10 mm/s
Hatch Travel Write Speed	12.7 mm/s
Layer Height	0.5 mm
Hatch Spacing	0.75 mm
Shielding Gas	Argon

3.1.5 High Velocity Air Sprayed WC-Co

While WC-Co can be deposited by variety of thermal spray technologies, high velocity air fuel (HVAF) was used to deposit this material as a conventional technique in this study. The HVAF deposition was carried out using a hybrid HVAF and high velocity oxygen fuel (HVOF) system by Kermetico, CA, USA. Coating coupon samples were deposited on a 75 (L) × 75 (W) × 5 (H) mm H13 substrate. The surface of the substrate was subjected to a sandblasting process prior to spraying in order to increase the adhesion between the substrate and the coating. An approximately 800 μm coating was deposited using the spraying process parameters listed in Table 4. EDM was again used to cut the sprayed parts into 40 x 5 x 5 mm samples for mechanical testing.

Table 4. Process parameters for HVAF spraying in this study.

Process Parameter	Value
Spray Distance	177.8 mm
Powder Feed Rate	200 g/min
Fuel (Propane) Flow Rate	90 L/min
Carrier Gas flow rate	23 L/min
Air Pressure	620-628 kPa
Nozzle Length	15.1 mm
Traverse Speed	900 mm/s

3.1.6 Material Composition of WC-Co

The same powder feedstock supplied by Kermetico Inc. was used for both the DED and conventional WC-Co samples. These powders had a nominal size of -30+5 μm and contained coarse carbides. The material composition of the powders is listed in Table 5.

Table 5. Composition of WC-Co alloy powders.

Element	W	Co	C	O
Weight %	Balance	15-18	4.9-5.3	0.01-0.2

3.2 Microstructural Characterization

All samples were cross-sectioned and mounted in conductive epoxy resin using an automatic mounting press prior to microstructural observation. The samples were then ground and polished using a Met Prep 3 by Allied High-Tech Products, Inc., USA. Following this, both CoCr samples were etched in a 1:3 solution of 70% nitric acid and hydrochloric acid for grain boundary observation. The WC-Co samples were etched in an aqueous solution of 30% nitric acid. A Zeiss Axiovert 40 MAT by Focus Precision Instruments, MN, USA was used for optical microscopy (OM) and porosity measurements. A more precise microstructural observation was conducted using scanning electron microscopy (SEM) by a JEOL JSM-6490LV by JEOL

(Peabody, MA, USA). This SEM was also equipped with an energy dispersive spectroscopy (EDS) detector capable of detection of elemental chemical composition of the samples.

3.3 Mechanical Testing

3.3.1 Micro Indentation Test

Vickers and Knoop micro indentation testing experiments were performed using a Clark CM-800 AT, according to ASTM E92-17 to determine the hardness of the samples in this investigation [33]. While a Vickers test is a reliable method for hardness measurement in metallic structures, a Knoop indentation test was also performed to support the analytical prediction of mechanical properties. In addition, due to relatively high surface area of its indenter, the Knoop method is capable of covering more microstructural features in layered type structure, such as DED processed samples. A comparison of Vickers and Knoop hardness indenters is shown in Figure 2. All hardness tests were performed sporadically on the cross-section of the samples. Both the DED and the conventionally processed samples were subjected to a 200 gf load at 15 s dwell time. The average hardness value was calculated from eleven random indentations on random regions of each sample.

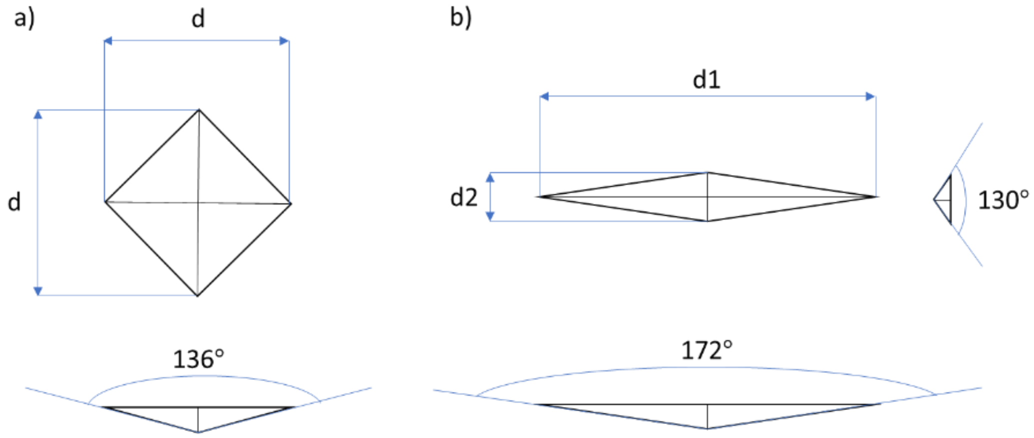

Figure 2. Schematic of a) Vickers and b) Knoop microhardness indenters.

3.3.2 Resonance Frequency

Resonance frequency testing, also known as impulse excitation, is an alternative method for measuring tensile properties of thin and small samples. It is a non-destructive test capable of accurately measuring mechanical properties such as shear modulus, elastic modulus, and Poisson's ratio [27, 28]. Due to the size restriction of the DED processed samples, preparation of sub-sized tensile test samples and conducting tests on those small samples seemed like a challenging task. The accuracy of the results would also be under question due to the sensitivity of such small samples due to any misalignment during tensile test. Furthermore, resonance frequency testing has the capability to conduct multiple measurements on a singular sample. Because of these reasons, resonance frequency testing was used as an experimental method to measure the Young's moduli of the samples in this study. The resonance frequency test was conducted five times on free-standing samples of both materials. The results provided measured mechanical properties in the longitudinal direction which simulates the application of in-plane tension similar to a tensile test. This study was conducted according to ASTM E1876-99 by IMCE, Belgium [36]. In this test, a hammer (impulser*)* continuously tapped on one side of the sample and the produced sound was constantly recorded on the other end of the sample using a highly sensitive microphone (transducer) as schematically replicated in Figure 3. A resonance frequency data analyzer (RFDA) was then used to convert the vibration signals from the recorded sounds into mechanical properties and constants.

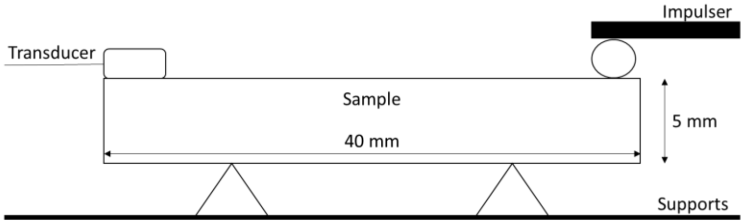

Figure 3. Schematic of the resonance frequency test setup.

4. RESULTS

4.1 Microstructure Characterization

4.1.1 SEM and EDS Analysis of CoCr

Microstructural characterization was conducted to better address the mechanical behavior of the CoCr samples using specific microstructural features. Several SEM micrographs have been taken randomly from microstructure of both the DED and conventional CoCr samples in order to fully analyze this sample. SEM micrographs shown in Figure 4 indicated that microstructure of the DED processed CoCr sample contains a large variation of grain size with different morphologies compared to the conventionally processed sample. The dominant microstructure of the DED processed sample was fine cellular grains surrounded by boundaries along melting pools. However, regions of different sizes of equiaxed and columnar grains were also observed as seen in Figure 4 (a). The inset of Figure 4 (a) clearly illustrates melt pools within the microstructure of the etched cross-section of the DED processed CoCr sample, which is typical for a 3D printed metallic sample. The horizontal overlap of the melt pool boundaries showed the deposition pattern and direction during the buildup process. The wide variation in grain size, shape, and orientation are among typical characteristics of AM metallic materials [30, 31]. In contrast, the conventionally processed sample had a dominant equiaxed grain structure throughout the sample with little variation as shown in Figure 4 (b).

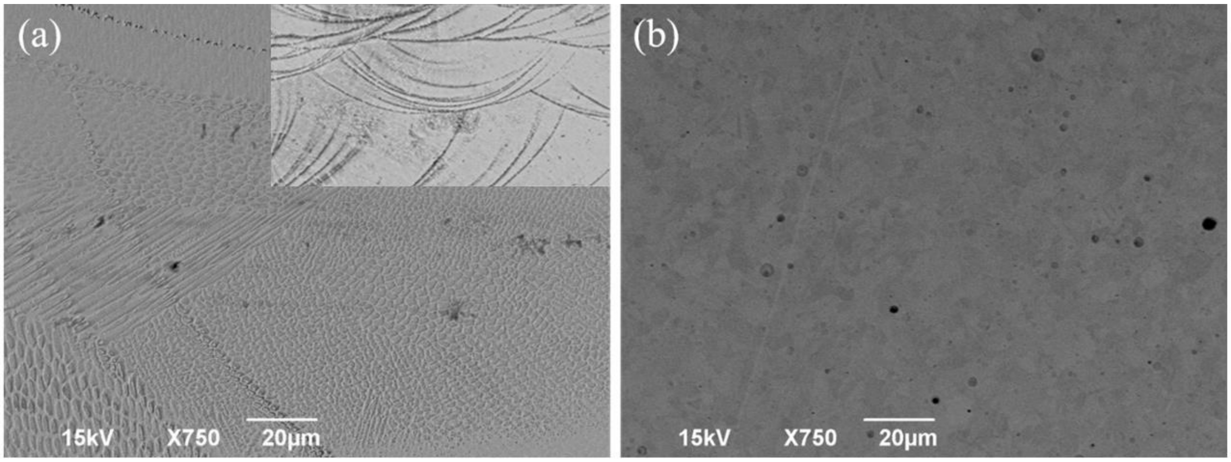

Figure 4. SEM micrographs of the cross-sectional regions of the (a) DED processed and (b) conventional CoCr samples. Inset of (a) shows melt pools in the DED processed samples at different magnification.

EDS analysis determined elemental composition of both the DED and the conventional samples, as listed in Table 6. The cobalt content is slightly lower for both samples compared to the values reported by the manufacturers, as previously shown in Table 2. The SEM micrographs of both samples do not show noticeable amounts of pores, defects, or cracks in the microstructure of both samples. Porosity measurements performed on unetched samples using OM revealed porosities of approximately 0.2% and 0.1% in the DED and conventionally processed CoCr samples, respectively.

Table 6. Chemical composition by EDS for DED and conventionally processed CoCr alloy samples in this study.

	Element (wt%)			
	Co	**Cr**	**Mo**	**C**
DED	60.84 ±2.79	29.50 ±1.24	6.62 ±0.51	1.53 ±0.23
Grain	64.30±2.88	28.57±0.87	4.68±0.49	1.20±0.16
Boundaries	58.94±2.80	29.78±0.90	7.66±0.78	1.07±0.16
Conventional	63.17 ±2.69	28.90 ±1.20	5.34 ±0.69	0.94 ±0.15
Light	63.82±2.79	28.18±1.21	5.33±0.49	1.11±0.21
Dark	62.72±2.73	28.44±0.63	5.65±0.70	1.29±0.16

4.1.2 SEM and EDS Analysis of WC-Co

Microstructural characterization was also completed on the DED and HVAF processed WC-Co samples in order to better understand the specific microstructural features that can influence their mechanical behavior. Several SEM micrographs have been taken randomly across each sample in order to capture all of the microstructural features. SEM micrographs of the DED sample shown in Figure 5 depicted a very chaotic and inhomogeneous microstructure. On account of the distinct regions of the sample that possess different microstructural characteristics, the DED sample was separated into top (T), middle (M), and bottom (B) regions, each consisting of roughly 250 μm of height. A large variety of carbide sizes seemed to be present throughout the sample and no distinct boundary can be observed between the WC-Co and the H13 substrate. Dark circular features mostly visible in the middle of the sample have been identified as cobalt rich phases. The bottom area consisted of a mixture of iron and WC-Co, as the H13 steel substrate melted due to the high temperature generated during the DED process. This has also been reported by others in literature for the same material produced by AM technology [39], [40]. The HVAF coating, on the other hand, appears homogeneous and shows a distinct interface with the substrate, indicating no mixing occurred between coating and the substrate. The measured porosity using image analysis were 4.08 and 0.72 area percentage for the DED and HVAF deposited samples, respectively.

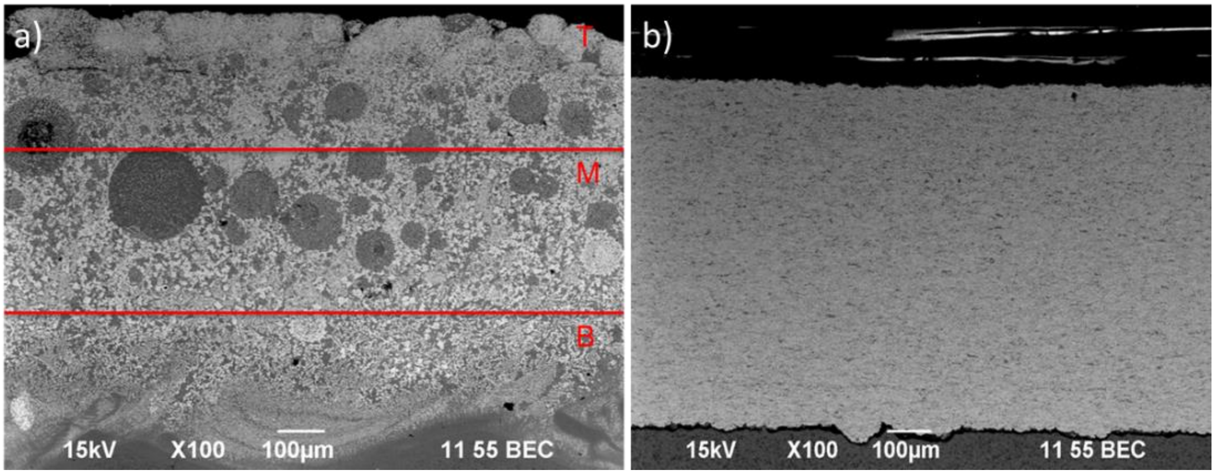

Figure 5. SEM micrographs of (a) the DED WC-Co sample and (b) the HVAF deposited WC-Co sample.

In order to further investigate the iron content, EDS was conducted on each region of the DED sample separately as well as on the entirety of both the DED and HVAF samples. The elemental composition analysis by EDS for each region shown in Figure 5 (a) are listed in Table 7. It is clear that due to the melting and mixing of the substrate into the WC-Co material, the bottom and middle regions have large concentrations of iron in their composition. This also causes a steep decline in the amount of tungsten-carbide in these areas. The iron content appears to decrease drastically in the top region of the DED processed WC-Co sample. Due to this affect, the overall composition of the DED sample contains more than 20% iron, which is an undesired effect of this method of manufacturing on the composition of the sample. The EDS results indicated that HVAF coating sample contains no traces of H13 substrate.

Table 7. Chemical composition of WC-Co by EDS.

	Element (wt%)			
	W	**Co**	**Fe**	**C**
DED Total	58.06±0.18	11.75±0.10	22.25±0.11	4.92±0.02
Top 250 μm	68.42±0.18	10.76±0.09	13.19±0.08	5.65±0.03
Middle 250μm	57.36±0.18	14.10±0.10	24.29±0.11	4.69±0.02
Bottom 250μm	54.92±0.17	9.99±0.09	26.67±0.12	4.81±0.02
HVAF	71.00±1.29	22.59±1.66	0	3.57±0.28

4.1.3 Analytical Model Based on Microstructural Features

A well-known analytical scheme that can establish a relationship between microstructural features and mechanical properties of materials with layered structure has been developed by Hashin-Hasselman [32, 33]. This is the most widely used theoretical relation between porosity and elastic modulus, and is given by:

$$E = E_0 \left[1 + \frac{Ap}{1 - (A + 1)p}\right] \tag{1}$$

where E_0 is the bulk elastic modulus, A is a constant equal to -33.4, and p is the porosity of the sample. For CoCr, E_0 is assumed as 220 GPa [43]. For WC-Co, E_0 is based on applying the rule of mixtures (RoM) to the overall material composition of each sample. This is shown in Equation 2 in which v_i is the volume fraction of each element calculated from the EDS results and E_i is the elastic modulus of each material.

$$E_{tot} = v_1 E_1 + v_2 E_2 \ldots \tag{2}$$

The elastic moduli for each material component were acquired from the AZoM database [44]. This resulted in the DED WC-Co possessing a bulk modulus of 427.97 GPa, while the HVAF deposited WC-Co sample's bulk modulus was 495.54 GPa.

Based on the 0.2% and 0.1% porosity content of the DED and HVAF processed CoCr samples previously mentioned in this study, application of Equation 1 resulted in elastic moduli of 206.20 GPa for the DED processed CoCr sample and 212.88 GPa for the conventionally processed CoCr sample. Based on the porosity contents of 4.08% for the DED WC-Co sample and 0.72% for the HVAF processed WC-Co sample, the Hashin-Hasselman model resulted in elastic moduli of 269.69 GPa and 398.91 GPa for the DED and HVAF deposited WC-Co samples.

4.2 Mechanical Results

4.2.1 Microindentation

The indentation test on the DED and conventionally processed samples was performed on the cross-section and surface of each sample in both the longitudinal and transverse directions to obtain more accurate average results for each sample. The average Knoop hardness of the DED CoCr samples was 438.28 ± 33 HK, while the hardness for conventionally processed samples was 469.30 ± 30 HK. The higher hardness value in conventionally processed samples could be attributed to its relatively lower porosity content. The possibility of better metallurgical bonding between materials (grains) through the solidification process in conventional samples could be another reason for exhibiting higher hardness. A wide range of hardness values were reported for CoCr alloys fabricated by different manufacturing techniques, from 372 HK for as-cast CoCr samples used for dental implants [45], to 650-700 HK of heat-treated ones [46]. To validate the Knoop hardness results, a set of Vickers hardness tests was also performed on each sample. The average Vickers hardness of the DED and conventionally produced samples were 457.7 ± 14 HV and 518.1 ± 17 HV, respectively. A similar relationship can be seen between the Vickers hardness values and the ones obtained from the Knoop microindentation test. It has also been shown that the measured hardness of the DED processed sample in this study is higher than the range of hardness values reported in literature [37, 38].

The average Knoop hardness for the DED WC-Co sample was 1398.67 ± 25.53 HK, while the HVAF deposited samples had a Knoop hardness of 1101.21 ± 20.03 HK. Other additively manufactured WC-Co samples have been found to have a Knoop Hardness of 920-1120 HK [49]. Knoop hardness values for similar compositions of thermally sprayed WC-Co have been shown to be in the range of 1000-1100 HK [50]. Vickers hardness tests were also performed on the sample in order to validate the Knoop hardness, and resulted in 1493.69 ± 83.9 HV and 1162.90 ± 52.7 HV microhardness averages for the DED and HVAF deposited WC-Co samples, respectively.

4.2.2 Analytical Model Based on Knoop Hardness

Another commonly used analytical model for estimation of the elastic modulus of metallic materials was developed by Marshall as shown in Equation 3 [51]. This model relates the modulus of elasticity to the Knoop hardness value obtained from microindentation tests using the equation:

$$E = \frac{\alpha * HK}{\frac{b}{a} - \frac{b'}{a'}} \tag{3}$$

Here, a and b are half of the long and short diagonals of the indenter and a' and b' are half of the measured long and short diagonals of the indent left on the sample. HK is the measured Knoop hardness and α is a constant that is theoretically 0.34 [39, 40]. This model can also be used as an empirical approach in which α is adjusted to known values. The ratio of a and b is also considered a constant according to the ASTM standard for the Knoop indenter [33]. The major and minor diagonal angles are required to be 172.5º and 130º, which in turn leads to Equation 4.

$$\frac{b}{a} = \frac{\tan\left(\frac{172^\circ}{2}\right)}{\tan\left(\frac{130^\circ}{2}\right)} = \frac{1}{7.1144} \tag{4}$$

The calculated elastic moduli for the DED and conventionally processed CoCr samples were 203.13 ± 45.76 GPa and 196.91 ± 59.57 GPa respectively by application of Marshall equation. The elastic moduli for the WC-Co samples from the use of the Marshall model were 292.05 ± 38.07 for the DED sample and 347.03 ± 73.05 for the HVAF sample.

4.2.3 Resonance Frequency

Due to the size limitations for DED processed samples and thermal sprayed ones, resonance frequency testing, also known as *impulse excitation*, was employed to examine mechanical properties of the samples in the transverse direction perpendicular to the build-up process. The average elastic modulus of a free-standing DED CoCr sample was determined to be 270.56 ± 0.01 GPa while the measured value obtained for the conventionally fabricated one was 228.41 ± 0.00 GPa. The calculated standard deviations were negligible for both samples corresponding to high accuracy of the experiment. It is worth mentioning that one sample could be examined for this test and repeating the test on one sample is only for checking accuracy of the test and results. The resonance frequency test showed an outstanding elastic modulus for DED processed CoCr sample: approximately 16.9% higher than the one obtained for conventionally produced sample in this study and in literature. Since resonance frequency simulates stress-strain condition in uniaxial directions, it seems that layered structures with strong interface could show higher strength when loaded transverse to printing direction. Similar mechanical behavior has already been reported for longitudinally aligned metal matrix composites [53]. The results indicate the in-plane strength of the samples are similar to the strength obtained from the tensile test found in literature [34, 42]. A previous study showed that typical elastic modulus for CoCr material regardless of manufacturing method was in the range of 200-253 GPa [55]. Another specific study on additively manufactured CoCr sample by SLM technology reported elastic modulus of 213 GPa [56].

Generally, AM processed metallic samples have shown lower mechanical strength compared to conventionally fabricated ones. However, some previous literature has shown that the tensile properties of AM fabricated parts can be compared favorably to those of conventionally produced ones. This happened when porosity distribution between printed layers was minimized by optimization of printing orientation and process parameters [57]. The work of Dongare *et. al.* also showed that materials fabricated through AM can have increased tensile properties when compared to conventionally processed ones in terms of having optimum grain orientations. However, their main purpose was not to provide a comparison between the mechanical and microstructural properties of AM and conventionally processed samples, and to this end, there is no detailed study reported in this particular area [58].

Resonance frequency testing was also conducted on the both WC-Co samples in this study. The HVAF deposited sample was separated from the substrate using EDM and tested as a free-standing coating. However, it was not possible to perform the same operation to separate DED processed WC-Co samples from the substrate since they shattered in all attempts. This could be due to the mixing of the H13 substrate and the WC-Co as discussed previously. Because of this, the DED WC-Co samples were subjected to the resonance frequency test attached to the H13 substrate. To calculate the elastic modulus of the DED processed section, an uncoated H13 sample was also subjected to the resonance frequency to be able to use the Pautrot model shown in Equations 5-8 [59].

$$E_t I_t = E_s I_s + E_c I_c \tag{5}$$

$$I_s = \frac{bh_s^3}{12} + bh_s\left(\frac{h_s}{2} - e\right)^2 \tag{6}$$

$$I_c = \frac{bh_c^3}{12} + bh_c\left(\frac{h_c}{2} + e\right)^2 \tag{7}$$

$$e = \frac{E_s h_s^2 - E_c h_c^2}{2E_s h_s + 2E_c h_c} \tag{8}$$

Here, E_i is the elastic modulus, I_i is the second moment of inertia, b_i is the width, h_i is the height, and the subscripts s, c, and t represent the designation of the substrate, coating, and total sample, respectively. The shift of the neutral axis is expressed as the variable e and is represented in Figure 6. It should be noted that the thickness of the coating and substrate is assumed to be constant throughout the sample, although it has been shown in the SEM image in Figure 5 (a) that the boundary between these two regions is not definitive. The mixing that occurred between these two regions during the DED process could construe this value and potentially cause some error in the results obtained for the DED produced WC-Co sample. These nonlinear equations were then solved for the elastic modulus of the coating, E_c, using the Newton Raphson method. The computational code for this was input into MATLAB software and is included in Appendix A. This resulted in an elastic modulus of 156.02 ± 0.05 GPa and 353.82 ± 0.03 GPa for the DED WC-Co and free standing HVAF samples, respectively.

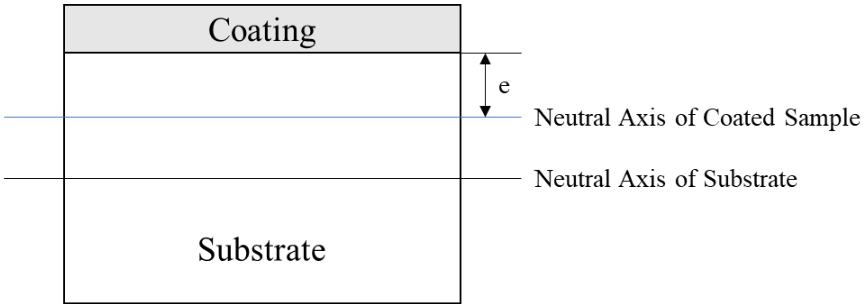

Figure 6. Shift of the neutral axis due to coating application

Additively manufactured WC-Co produced using SLM has been found to have an elastic modulus of 400.8 GPa [60]. Thermally sprayed samples with a similar composition have been shown to have an elastic modulus in the range of 200-300 GPa [61], [62]. It appears that the sample used in this study surpasses the expected range as reported in literature by a considerable amount. It is believed that the significant decrease in elastic modulus between the HVAF and additively manufactured WC-Co samples is due to the nonuniform microstructure and mixing of the iron from the substrate with the WC-Co material within the microstructure. This mixing caused a plethora of weak points at material interfaces which resulted in the formation of regions with higher stress concentrations. Furthermore, based on the EDS results, the existence of iron in the composition results in depletion of strong WC phase which could also contribute to the decrease in elastic modulus of DED processed sample.

5. OBJECT ORIENTED FINITE ELEMENT ANALYSIS

Finite element analysis (FEA) has been utilized in this study to estimate the tensile properties of the CoCr samples. If the results obtained from the FEA study fall within an acceptable range of the experimental values, it will provide a useful tool for the prediction of the performance of materials without the need for running costly and difficult physical experiments. The success of this numerical simulation method could also allow for the testing of many materials in which sample preparation is difficult. This is due to the ability of this method to analyze several samples from one specimen using SEM independent of mechanical tests.

5.1 Introduction to OOF

Object oriented finite element analysis (OOF) is an emerging numerical simulation methodology developed at the National Institute of Standards and Technology (NIST) to estimate materials properties. Unlike other finite element methods which heavily rely on modeling parts and components, OOF uses actual images randomly taken at different regions of the microstructure. This innovation allows the program to account for real microstructural features such as porosities, impurities, or multiple phases within a specific sample's microstructure. Each distinct contrast within the microstructure is characterized by its properties such as elastic modulus, Poisson's ratio, and coefficient of thermal expansion. This micromechanics scheme then allows for the simulation of mechanical or thermal stresses under given elastic conditions or temperatures.

The process starts with uploading a micrograph at optimum resolution and magnification into the program. Azarmi *et. al.*, explained the detail of the process for selection of optimum (threshold) resolution for micrographs used in OOF study [41]. The different phases within the microstructure among other microstructural features can be distinguished based on their color or contrast. In the next step, all micrographs are processed by applying property values to different features within the microstructure. As it is required for FEA study, the processed image will be discretized to elements and nodes to build a skeleton that can later be refined and annealed for higher accuracy and uniformity during the calculation. A skeleton is the term used in this program for the discretized and meshed image containing the elements, edges, and nodes. The homogeneity index of the skeleton refers to the average uniformity of all elements and ranges from 0 to 1. An element's homogeneity index is considered unity when it entirely encompasses one material, while it is less than one if the element is spread among multiple materials. The skeleton is refined until this index reaches a maximum possible value.

The final steps include designating the type of the desired analysis and specifying the boundary conditions for the analysis. Boundary conditions such as displacement, temperature, and voltage can be defined to create mechanical, thermal, and electrical equations. The program then solves these equations using finite element analysis concepts and returns the desired stress, strain, thermal, displacement, or voltage results.

Once all required steps are completed and the inputs are specified, the program can solve the appropriate equations. OOF is capable of graphically displaying the stress, strain, or thermal maps based on the solved equations on each node and element. A useful tool known as the analysis tab can display the results of a singular element, cross-sections of the image along a boundary, or average all elements within the entire skeleton. These results can also be displayed in a contour map in the graphics window.

5.2 Numerical Simulation of CoCr Samples

Figure 7 (a & c) shows a selected region of a micrograph that was cropped to a sample size of 150 μm in the longitudinal direction and 100 μm in the transverse direction. Pixels were designated as CoCr or pores. The area fraction of the porous regions was within one standard deviation of the measured porosity [41]. The CoCr pixels were given properties of 220 GPa for Young's modulus and 0.29 for Poisson's ratio [43], while pore pixels were assigned a Young's modulus equal to 1 Pa and a Poisson's ratio of 0.33 [41]. A skeleton of 90×60 triangular elements was generated and modified using the refine, anneal, and snap nodes functions until the homogeneity index exceeded 0.98. This homogeneity index was selected empirically due to the decrease in its improvement as a result of further skeleton refinement. Processed skeletons for the DED and conventional samples are shown in Figure 7 (b & d).

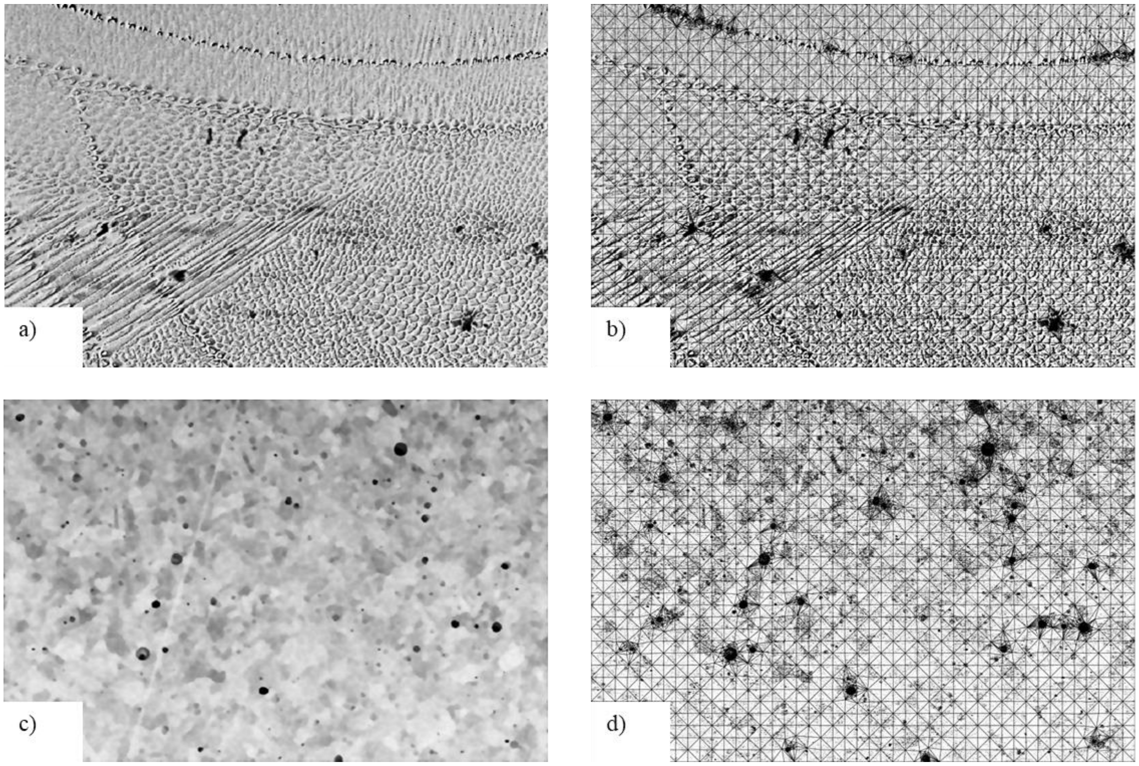

Figure 7. A cropped 150 x 100 μm micrograph of a) a DED fabricated CoCr microstructure, b) processed (meshed) OOF skeleton ready for analysis, c) a conventionally produced CoCr microstructure, and d) processed (meshed) OOF skeleton ready for analysis.

The displacement field was selected as the active field and a force balance equation was selected to solve for the mechanical elastic properties of the sample. The boundary conditions were set to fix the left edge in the longitudinal direction and the top and bottom edges in the transverse direction. The right edge was displaced 0.1μm in tension in the longitudinal direction to simulate the tensile testing condition. This small displacement was chosen to remain within the material's elastic limit. The simulation was set to solve the problem to a residual accuracy of 1×10^{-9}.

The simulations could be completed (solved) in a relatively short time, approximately ten minutes, and results indicated the average stresses of 199.74 MPa and 198.31 MPa for the DED and conventionally fabricated samples, respectively. A contour stress map for each sample was also generated to visualize the stress in the longitudinal direction as depicted in Figure. 8. The average stress was then used to calculate the Young's moduli of the samples. The plane stress approximation was simulated using Equation 9 to compensate for two dimensional (2D) micrographs.

$$E = \frac{\sigma_{xx}(1-\nu)}{\varepsilon_{xx}} \tag{9}$$

Here, σ_{xx} is the stress in the longitudinal direction, ν is the Poissons ratio of the material, and ε_{xx} is the applied strain. The Poisson's ratio of CoCr is 0.29 and the strain based on the applied deformation is 0.067%. The estimated elastic moduli of the DED and conventional samples were 212.73 GPa and 211.20 GPa, respectively.

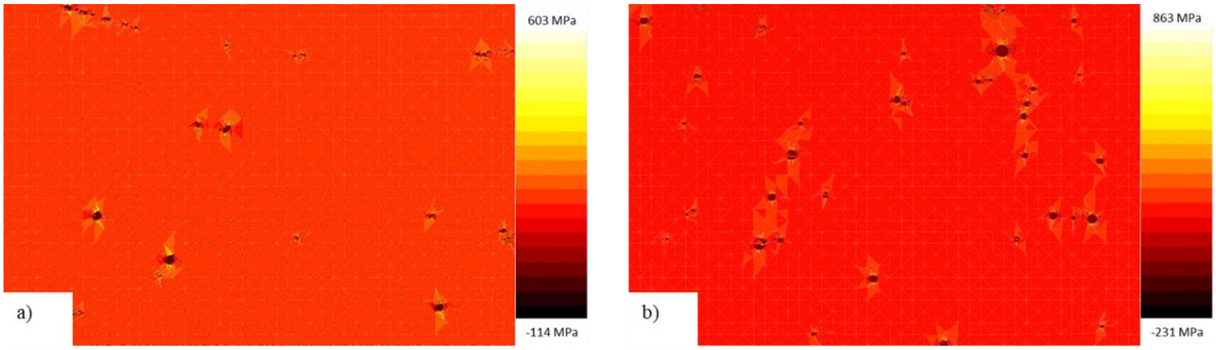

Figure 8. Stress maps created for the original OOF tensile simulation for a) the DED CoCr sample and b) the conventional CoCr sample shown in Figure 7.

It was decided that the homogenous designation of CoCr material and its properties did not accurately represent the microstructure. Instead, it produced an isotropic sample with little attention to the microstructural features besides the slight effect of the very low porosity content. To improve the accuracy, the rule of mixture was used for material property calculations based on the results obtained from the EDS study as previously presented in Table 6.

The material properties for each element were acquired from AZO Materials [44]. The DED sample was separated into grain and boundary designations, while the conventionally produced CoCr was separated into light and dark regions based on the visible contrasts, as seen in the SEM images. The calculated properties of these regions are shown in Table 5. The same skeleton generation process as previously shown in Figure 7 (a & c) are repeated using RoM method for martials properties as shown in Figure 9. Previously, the skeleton only considered two materials, CoCr and porosities, and was very basic as a result. With the addition of RoM, the skeleton can now account for the boundaries between three materials: the two contrasts of CoCr materials noted in Table 8 and porosities. The meshes were generated using the same process as described above, but are much more complex as a result of accounting for more features in the microstructure.

Table 8. Elastic modulus obtained from RoM for different contrasts in OOF simulation.

Area	RoM Elastic Modulus (GPa)
DED Grains	238.08
DED Boundaries	242.79
Conventional Light Region	238.78
Conventional Dark Region	238.91

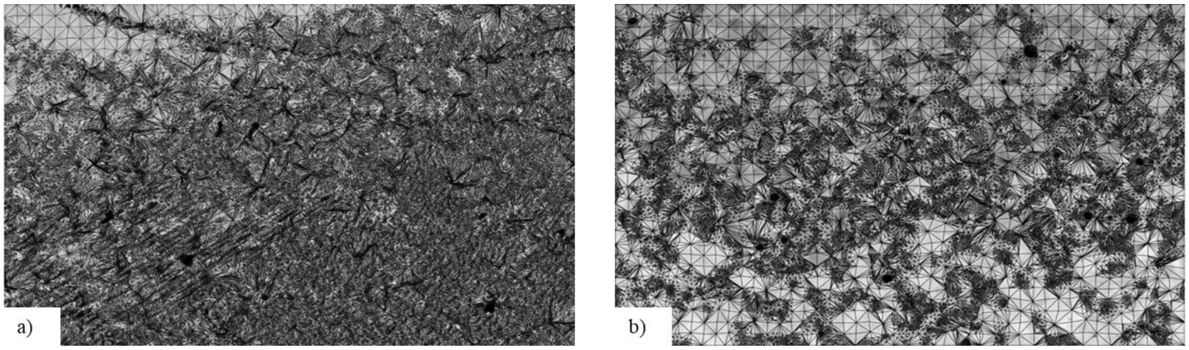

Figure 9. Processed (meshed) skeletons generated from the micrographs shown in Figure 7 using RoM properties for a) the DED CoCr sample and b) the conventional CoCr sample.

The same tensile test simulation process as described before was applied to the new meshed samples. The runtime for these simulations was longer (approximately 30 minutes). The contour stress maps are shown in Figure 10 for the OOF analysis using RoM material properties, which correspond to the processed images shown in Figure 9. The lighter contrast represents higher stress level in the microstructure that are centralized at the pores in both samples. Three micrographs of each sample of CoCr were examined in OOF using the same method described here. The calculated average stress from all the elements at displacement equal to 0.1µm in tension is listed in Table 9. The strain was again calculated as 0.067% based on the selected displacement and original dimensions of the sample. From these values, Young's moduli were calculated for the samples, as listed in Table 9.

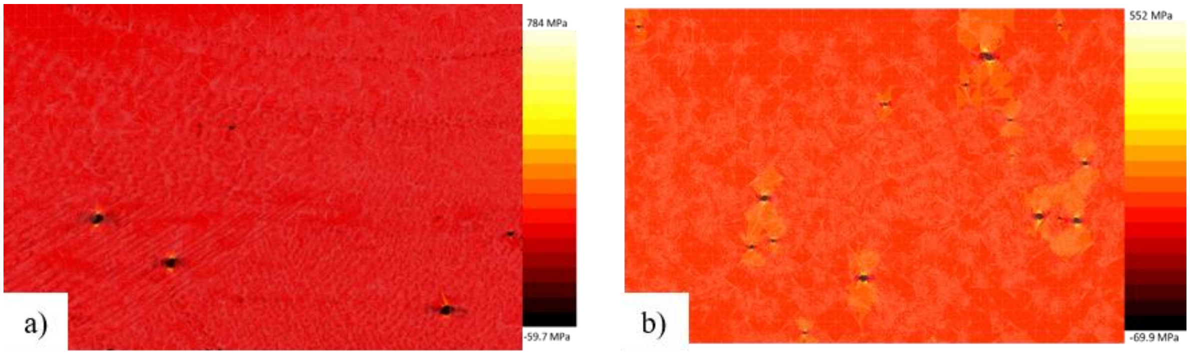

Figure 10. Longitudinal stress maps for a) the DED fabricated and b) the conventionally produced CoCr corresponding to the processed images shown in Figure 9.

Table 9. OOF Results from Simulation of Tensile Test.

Sample	Average Stress (MPa)	Elastic Modulus (GPa)
DED	206.41 ± 1.98	219.82 ± 2.11
Conventional	207.18 ± 0.56	220.65 ± 0.59

5.3 Numerical Simulation of WC-Co Samples

5.3.1 Resolution Optimization Study

To begin the OOF study on the WC-Co samples, a resolution optimization study was performed on the HVAF deposited sample. This study used micrographs taken at 100x, 500x, 1000x, and 2000x magnification to examine their influence in estimation of elastic modulus when subjected to the OOF analysis. An example SEM image taken at those magnifications are shown in Figure 11. A larger number of micrographs were used for higher magnification images in order to compensate for the smaller area covered by high magnification images. Specifically, three simulations at 100x, five simulations at 500x, seven simulations at 1000x, and nine simulations at 2000x magnification were performed in order to select the optimum resolution. The optimum resolution then will be used for OOF simulation of tensile properties of the WC-Co samples in this study. SEM micrographs at each magnification were cropped to a nominal sample size, shown in Table 10.

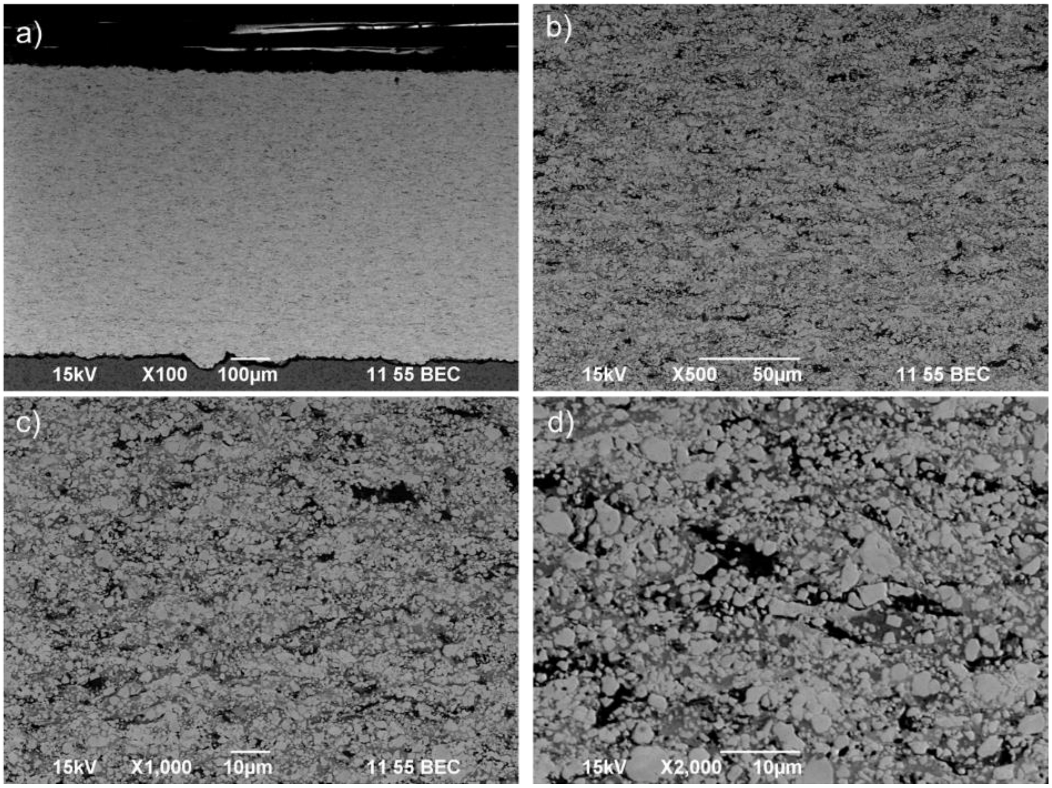

Figure 11. SEM Images of the HVAF deposited WC-Co sample taken at (a) 100x, (b) 500x, (c) 1000x, and (d) 2000x magnification.

Table 10. Sample size dimensions for OOF Simulation of HVAF deposited WC-Co.

Sample Magnification	**Dimensions (µm)**	
	Longitudinal	**Transverse**
100x	1000	500
500x	250	125
1000x	100	50
2000x	50	25

Pixels for each sample were designated as WC, Co, or pores based on their contrast. The area percentages of each material in the OOF simulation were monitored and compared with the

EDS results to ensure an accurate material designation. The materials were then given their corresponding properties as shown in Table 11 from the AZoM database [44]. It should be noted that in the 100x magnification samples, it is impossible to distinguish the carbides and cobalt from each other as seen in Figure 11 (a). To account for this, the pixels were designated into two material categories instead of three: WC-Co or porosities. The mechanical properties of WC-Co have been calculated using RoM on the EDS results for this sample.

Table 11. Mechanical properties of the materials used in OOF simulation of WC-Co.

Material	Elastic Modulus (GPa)	Poisson's Ratio
WC	643	0.21
Co	210	0.32
Pores	1×10^{-9}	0.33

An initial skeleton of 45×30 triangular elements was generated and refined as before in the CoCr simulations with the goal of a 0.95 homogeneity index. The homogeneity index goal is lower in these WC-Co samples as they have more features to account for, making a higher index much harder to achieve. An example of each fully refined skeleton is shown in Figure 12. It is seen that the 100x skeleton is much less complex than the other magnifications due to the simplification of only using only a singular WC-Co material. The mesh was then generated for each of the skeleton samples. The boundary conditions were set for each magnification so that the strain of each sample remained constant at 0.001. This kept each sample within its elastic range and imposed deformations of 1, 0.5, 0.1, and 0.05 μm in the longitudinal direction on the 100x, 500x, 1000x, and 2000x samples, respectively. The accuracy was set to 1×10^{-9} as before and the simulations were performed to simulate a tensile test condition.

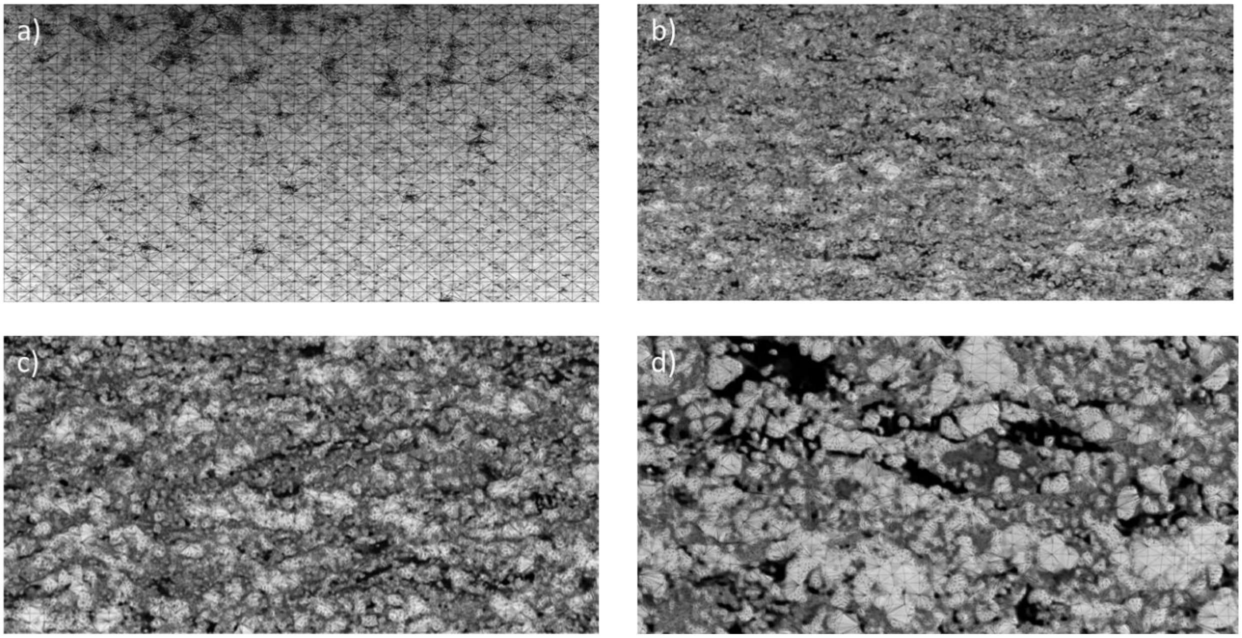

Figure 12. Refined skeletons for OOF analysis of the (a) 100x, (b) 500x, (c) 1000x, and (d) 2000x magnifications of the HVAF deposited WC-Co samples.

The simulations required a longer time to solve with increasing magnification. While the 100x micrographs were able to be solved in a small 10-minute runtime, the 2000x micrographs required approximately an hour to complete due to the increased number of features and therefor elements in the finite element mesh. An example of a stress map for each magnification sample is shown in Figure 13. The resulting average stresses for each sample were then input into the plane stress assumption of Hooke's law shown in Equation 9 with a Poisson's ratio (ν) of 0.25 calculated by RoM. The average resulting elastic modulus for each magnification of the HVAF deposited WC-Co sample is shown in Table 12. It is seen that the 500x, 1000x, and 2000x resolutions all produce errors less than 10% when compared to the experimentally obtained value of 353.82 ± 0.03. This indicates that any of these magnifications would be sufficient for the remaining simulations. However, it is known from the microstructural analysis that the DED processed WC-Co sample micrographs include very small features which cannot be distinguished at the 500x magnification. In addition, encompassing the entirety of the DED sample and its inhomogeneous microstructure using 2000x resolution would require a vast number of samples. As a result, the 1000x magnification was selected as the optimum resolution for this analysis.

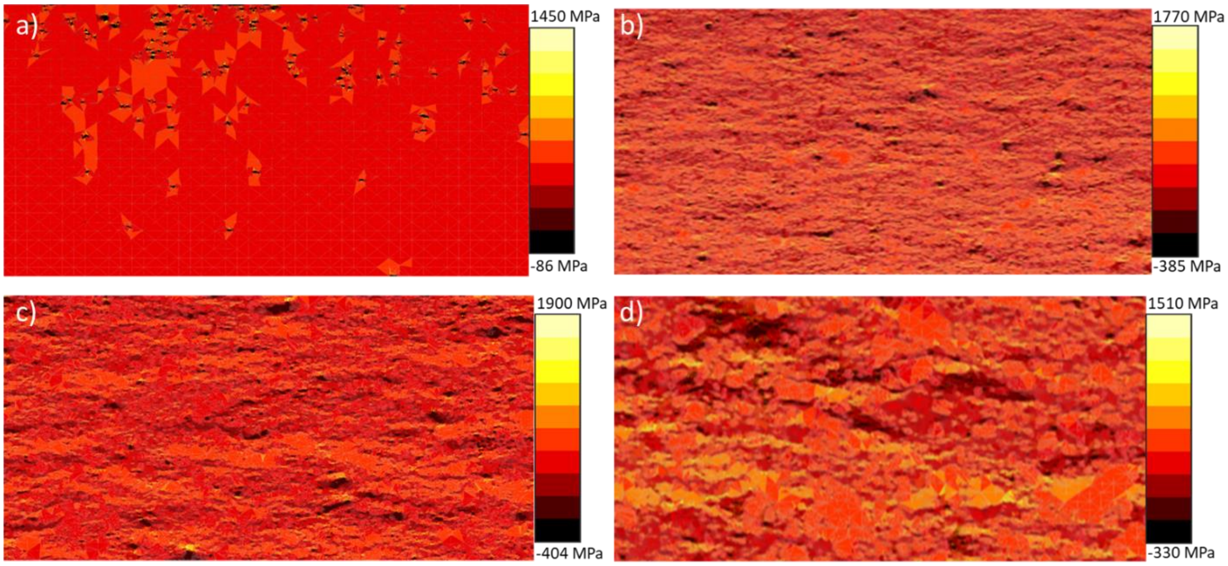

Figure 13. Stress maps created by OOF for the (a) 100x, (b) 500x, (c) 1000x, and (d) 2000x conventionally processed WC-Co samples.

Table 12. Resulting elastic moduli obtained from using micrographs at different resolution for the HVAF deposited WC-Co sample.

Sample Magnification	OOF Elastic Modulus (GPa)
100x	389.81 ± 2.75
500x	348.10 ± 3.88
1000x	330.24 ± 7.00
2000x	332.05 ± 11.30

5.3.2 Simulation of DED Processed WC-Co Samples

Due to the inhomogeneous and non-uniform microstructure, application of OOF was a more difficult task for the DED processed WC-Co compared to the HVAF deposited one. As a result, the OOF analysis of the DED sample was performed separately on each area shown in Figure 5 (a). As the iron mixed into the cobalt rich regions, the pixels in these samples were designated as either WC or “matrix” material. During this analysis, this matrix material encompassed the Fe, Co, and porosities of the DED samples. The rule of mixtures was used on the amounts of these elements obtained from EDS study for each region while also accounting for the porosity. It should be noted that the iron was given an elastic modulus of 200 GPa and Poisson’s ratio of 0.3 [44]. Because the composition of each matrix is different, this resulted in different properties for each region, which are shown in Table 13.

Table 13. Material properties calculated by RoM for each matrix region of the DED processed WC-Co samples.

Matrix Region	Elastic Modulus (GPa)	Poisson’s Ratio
Top	178.89	0.31
Middle	184.61	0.31
Bottom	184.09	0.31

Once the pixels were designated as WC or matrix and given the corresponding properties, the skeleton was generated and refined in the same manner as the HVAF deposited WC-Co samples. An example of an initial sample from each region of the DED WC-Co sample is shown in Figure 14 (a-c). The mesh was generated and the boundary conditions were set to displace the right boundary in tension 0.1μm to produce a 0.001 strain. The accuracy was again set to 1×10^{-9}. Examples of resulting stress maps for each region of the DED sample are shown with their corresponding refined skeletons in Figure 14 (d-f).

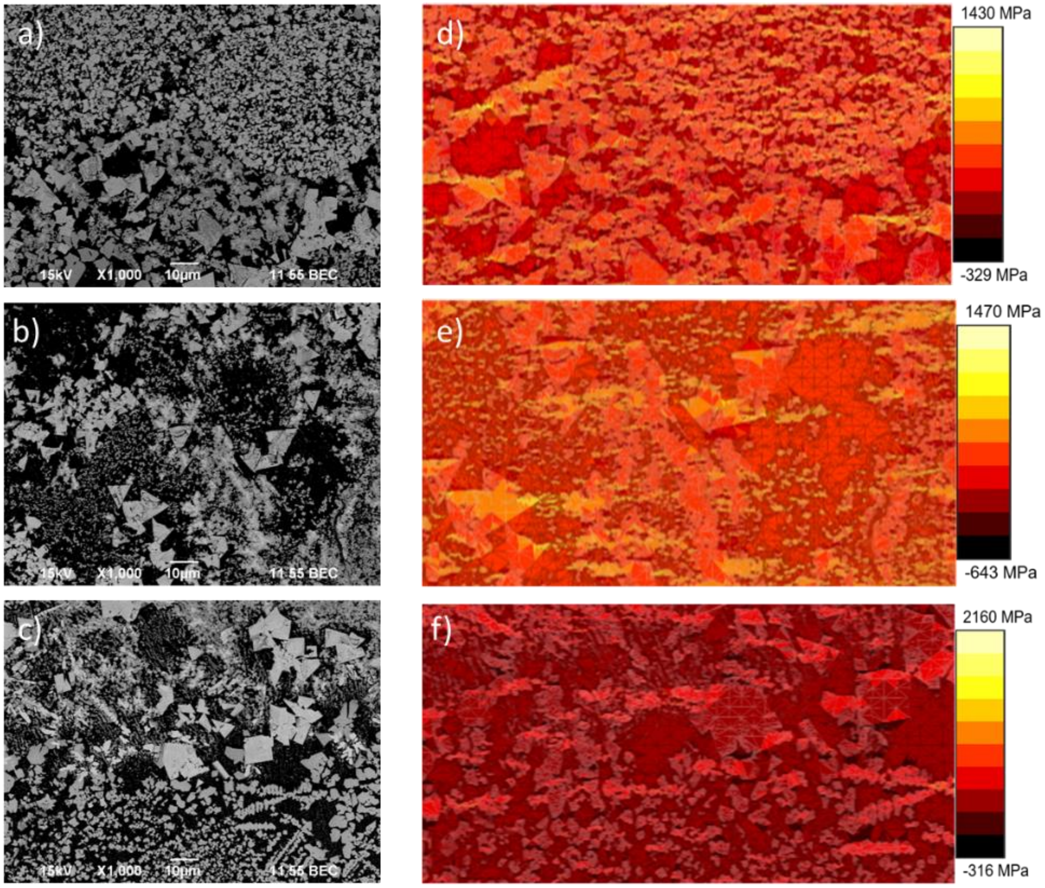

Figure 14. Initial SEM micrographs of (a) the top region, (b) the middle region, and (c) the bottom region of the DED WC-Co samples and their resulting stress maps (d-f).

As the microstructure of the DED sample is more complicated than the HVAF deposited one, more simulations needed to be conducted on this sample to encompass the differences in the various regions. Three randomly taken micrographs of each region of the DED processed sample have been simulated, and their results have been averaged within each region to calculate their respective results, and as a whole in order to estimate the results of the overall sample. These simulations required approximately one hour of solution time, similar to the 1000x HVAF WC-Co micrographs. The resulting stresses and elastic moduli of each area are shown in Table 14, as well as the average for the entire DED WC-Co sample from all of the regions. The higher elastic modulus in the HVAF deposited sample is as a result of two major factors. Primarily, it is due to the higher WC content in the HVAF deposited sample compared to the entire the DED processed sample according to EDS results shown in Table 7. This is due to depletion of WC due to diffusion of iron from the substrate mostly in to the bottom and middle regions marked in Figure 5 (a) and reported in literature [39], [40]. The samples then failed at lower stress levels in these regions due to containing more Co and Fe elements.

Table 14. Average stress and elastic modulus for the WC-Co samples resulting from OOF analysis.

WC-Co Sample	Average Stress (MPa)	Elastic Modulus (GPa)
DED Total	353.59 ± 24.60	265.19 ± 18.45
DED Top	385.37 ± 3.80	289.03 ± 2.85
DED Middle	337.56 ± 2.13	253.17 ± 1.60
DED Bottom	337.84 ± 11.34	253.38 ± 8.50
HVAF	440.32 ± 9.33	330.24 ± 7.00

6. DISCUSSION

Several experimental, analytical, and numerical studies were conducted on DED and conventionally manufactured CoCr samples to evaluate their elastic properties. Table 15 lists the elastic modulus obtained from each of the methods used on the CoCr samples to provide a better comparison. It is worth mentioning that this table is presented to provide a general comparison between the results and only includes standard deviations where applicable. The available range of data from literature has also been listed in the last row of the table to examine the accuracy of the results obtained in this study. While there is no specific report on elastic modulus of DED processed CoCr, conventionally made CoCr with 5% molybdenum has been shown to have an elastic modulus in the range of 210-230 GPa [34, 42].

Table 15. Summary of Elastic Modulus Results for the CoCr Samples.

Method	**Elastic Modulus (GPa)**	
	CoCr - DED	**CoCr - Conventional**
Resonance Frequency	270.56 ± 0.01	228.41 ± 0.00
Hashin-Hasselman (Porosity Content)	208.82	217.10
Marshall (Hardness)	203.13 ± 45.76	196.91 ± 59.56
OOF	219.82 ± 2.11	220.65 ± 0.59
Literature Review	-----	210-230

First, it needs to be noted that the resonance frequency test that provided experimental results could produce highly accurate results with negligible standard deviation, and thus it is used as the reference point in this study. Noticeably, all of the results obtained in this study for the conventionally processed CoCr fall within the acceptable range except the one from the application of the Marshall equation. This indicates the capability of all these methods to predict a relatively accurate elastic modulus in conventionally processed metals and alloys where there is more homogeneity and uniformity in the microstructure.

The Hashin-Hasselman theory is based on the porosity content of the microstructure and the theoretical elastic modulus of CoCr was considered as 220 GPa for the calculations. Since microstructural observation showed a higher level of porosity for the DED sample, it is speculated that the Hashin-Hasselman model shows lower elastic modulus in this sample. Due to the very low amount of porosity in both samples, very little deviation from theoretical elastic modulus can be seen (less than 10%). However, the analytical model suggested by Hashin-Hasselman was not capable of correctly estimating the elastic modulus in the DED processed CoCr sample with an anisotropic and lamellae type microstructure where different layer of the material can act as reinforcement phase and strengthen the material when load is applied in the transverse direction.

Marshall's method works based on the measured Knoop hardness and the dimensions of the large and small diagonals of the corresponding indents. The main source of the error in this equation, as indicated in other literature, is the fact that the size of small diagonal has no effect on hardness measurement but can significantly alter calculation of elastic modulus in Eq.2. Another source that shows the inability of the Marshall equation to accurately calculate the elastic modulus could be using 0.34 for the constant parameter (α) in Eq.2. This is the most widely accepted value, however some other reports have also used values such as 0.45 and 1.5 [52]. As a conclusion, analytical models could predict elastic modulus with less than 10% error from the actual experimental measurement for conventionally processed CoCr sample while this error could reach up to 40% for DED processed sample.

The numerical simulation study (OOF) resulted in relatively closer estimates for the elastic moduli of both samples than the analytical methods. This is attributed to the fact that in the numerical simulation, the model of the samples was pulled in uniaxial directions, which better resembles tensile test, while available analytical models mostly use general material properties to calculate the elastic modulus. Additionally, the OOF simulation was able to use actual microstructural images taken of the DED processed AM sample, which helped to perform a more accurate simulation. The numerical simulation method used in this study could accurately calculate the elastic modulus within 5% of the experimentally measured values for the conventionally fabricated CoCr sample.

On the other hand, the errors obtained from using OOF for DED processed CoCr sample were in the range of 10-18%. While OOF uses the actual microstructure, it seems that the selected resolution was not the optimum choice to clearly represent the features of individual layers as well as the detail characteristics of the interfacial area between layers. It is important to note that although using higher magnification micrographs could better reveal features such as interlayer boundaries, it could only represent a very small region of the microstructure and results could not be generalized for the whole material. Using a lower magnification would result in the opposite effect in which a larger region of the microstructure could be used but results in loss of important microstructural features.

The elastic modulus of WC-Co samples obtained from the application of different methods used in this study are listed in Table 16. As mentioned before, the results obtained from the resonance frequency experimental method is used as the reference point in this study due to its high level of accuracy. It must be mentioned that the results obtained for DED processed WC-Co sample are significantly lower than expected. This could be due to the iron diffusing into the coated region. Some error may also be due implementation of the Pautrot model, which calculated the elastic modulus of the coated section utilizing the assumption that the substrate and coating maintained constant thicknesses throughout the sample. It appears that each of the methods used in this study to approximate the elastic modulus of the samples produced a fairly accurate result for the HVAF deposited WC-Co sample. Only the Hashin-Hasselman method based on its porosity content produces more than a 10% error when compared to the resonance frequency testing. This indicates that all of these methods can provide reasonably accurate estimations for the elastic modulus of the samples with homogenous microstructures.

Table 16. Summary of elastic modulus results for the WC-Co samples in this study.

Method	**Elastic Modulus (GPa)**	
	WC-Co - DED	**WC-Co - HVAF**
Resonance Frequency	156.02 ± 0.05	353.82 ± 0.03
Hashin-Hasselman (Porosity Content)	269.69	398.91
Marshall (Hardness)	292.05 ± 38.07	347.13 ± 73.05
OOF	265.19 ± 18.45	330.24 ± 7.00
Literature Review	-----	200-300

The results diverge aggressively for the DED processed WC-Co sample. All three methods failed to accurately estimate elastic modulus of the DED fabricated sample when compared to the results obtained from resonance frequency test. The Hashin-Hasselman method utilizes the bulk modulus of the sample which was calculated by the RoM equation based on the EDS obtained composition results. In the HVAF deposited WC-Co sample, this method produces the highest error due to the low porosity of less than 1% causing little deviation from the bulk modulus. Although the use of the RoM equation was designed to estimate a more accurate bulk modulus it still contains a high error in both WC-Co samples. Considering the DED sample, the high iron content from the substrate greatly impacted the bulk modulus value, causing the result to deviate farther from the experimentally obtained elastic modulus of the sample.

The Marshall method based on the Knoop microhardness was able to provide the closest result for the HVAF deposited WC-Co sample. However, looking at the large standard of deviation, it can be seen that the results are still very scattered and inaccurate. This is due to the small diagonal of the indenter in Knoop hardness test still having a considerable effect on the calculation of elastic modulus but having no impact on the Knoop microhardness value itself. In the DED WC-Co sample, this value is once again far from the resonance frequency result. Because the indentation is performed on the cross section of the samples, the effect of the H13 substrate mixing with the sample can have varying effects on the indentation and measurements depending on the region in which the indenter landed on the microstructure.

The image based finite element simulation method provided a close estimate for the HVAF deposited WC-Co sample due to its uniform and homogenous microstructure. The use of the actual microstructure of the sample allowed the simulation to provide more accurate results than the analytical methods based on the general material properties of the sample. This allowed the simulation to accurately monitor the material composition and porosity of the samples to maintain proximity to the EDS results, causing the simulation to produce a result within 10% of the resonance frequency value.

OOF was able to model each region of the DED processed WC-Co sample and account for the varying iron content in each area. However, the inhomogeneous microstructure of the DED WC-Co sample was the main reason that OOF was unable to effectively estimate the elastic modulus. The simulation was able to incorporate the iron content by using RoM on the matrix material, but this method was still ineffective to account for the effect of the large iron presence and nonhomogeneous microstructure of the additively manufactured sample. This study does find that the current two-dimensional OOF is accurate on estimating the tensile properties of uniform samples with homogeneous microstructures, but as of now still lacks the capability to estimate the elastic modulus of materials with complex microstructure.

7. CONCLUSION

In this study, a series of analytical and numerical methods were examined to estimate tensile properties of cobalt chromium (CoCr) and tungsten carbide 17% cobalt (WC-Co) additively manufactured (AM) using direct energy deposition technique (DED). All measurements were repeated on a conventionally processed samples of both materials for the reason of comparison. All calculated values were evaluated and compared to the experimental studies performed on each sample to better understand the accuracy of those numerical and analytical methods. It has been shown that analytical methods using porosity content and hardness could provide reasonable approximations for the tensile modulus of a conventionally produced CoCr and WC-Co samples. This could be attributed to high uniformity in the microstructure of the conventionally processed samples. These estimations became more scattered when attempting to approximate the tensile properties for the DED processed samples. The numerical simulation of OOF provided the closest results to the experimentally measured ones for the DED sample. However, these results still were not within a reasonable accuracy when compared to the experimental resonance frequency results. This indicates that although OOF is an emerging numerical method to estimate the mechanical properties of materials with homogenous microstructure, further improvements are needed before it can reliably be used for materials with nonuniform and inhomogeneous microstructures.

8. FUTURE WORK

Further research should focus on the mechanical and microstructural properties of DED produced materials. Although the DED processed CoCr contained minimal cracks and pores, the DED processed WC-Co sample contained many flaws and undesired microstructural features. These greatly affected its mechanical performance and the simulation methods used here. Future studies could examine different printing parameters and whether these can improve the homogeneity and relative density of this AM material.

Investigation could also be performed into the accuracy of additional methods of simulating the tensile properties of a sample with minimal mechanical testing. NIST is currently in the process of developing and testing a three-dimensional version of OOF known as OOF3D. This has the potential to improve on the accuracy of the current version and to better simulate a physical sample. As other technologies are invented to estimate the tensile properties of a sample more accurately, these will also require comparison with existing methods.

REFERENCES

[1] H. Fayazfar *et al.*, “A critical review of powder-based additive manufacturing of ferrous alloys: Process parameters, microstructure and mechanical properties,” *Mater Des*, vol. 144, pp. 98–128, Apr. 2018, doi: 10.1016/j.matdes.2018.02.018.

[2] S. Natali, A. Brotzu, and D. Pilone, “Comparison between Mechanical Properties and Structures of a Rolled and a 3D-Printed Stainless Steel,” *Materials*, vol. 12, no. 23, p. 3867, Nov. 2019, doi: 10.3390/ma12233867.

[3] K. S. B. Ribeiro, F. E. Mariani, and R. T. Coelho, “A Study of Different Deposition Strategies in Direct Energy Deposition (DED) Processes,” *Procedia Manuf*, vol. 48, pp. 663–670, 2020, doi: 10.1016/j.promfg.2020.05.158.

[4] U. M. Dilberoglu, B. Gharehpapagh, U. Yaman, and M. Dolen, “The Role of Additive Manufacturing in the Era of Industry 4.0,” *Procedia Manuf*, vol. 11, pp. 545–554, 2017, doi: 10.1016/j.promfg.2017.07.148.

[5] X. Zhai, L. Jin, and J. Jiang, “A survey of additive manufacturing reviews,” *Materials Science in Additive Manufacturing*, vol. 1, no. 4, p. 21, Nov. 2022, doi: 10.18063/msam.v1i4.21.

[6] ASTM International, “ISO/ASTM 52900: Additive Manufacturing-General Principles-Fundamentals and Vocabulary,” 2021.

[7] X. Zhang, W. Li, and F. Liou, “Additive manufacturing of cobalt-based alloy on tool steel by directed energy deposition,” *Opt Laser Technol*, vol. 148, Apr. 2022, doi: 10.1016/j.optlastec.2021.107738.

[8] W. Yuan, X. He, X. Zhou, and Y. Zhu, “Hydroxyapatite Nanoparticle-Coated 3D-Printed Porous Ti6Al4V and CoCrMo Alloy Scaffolds and Their Biocompatibility to Human Osteoblasts,” *J Nanosci Nanotechnol*, vol. 18, no. 6, pp. 4360–4365, Jun. 2018, doi: 10.1166/jnn.2018.15207.

[9] S. Acharya, R. Soni, S. Suwas, and K. Chatterjee, “Additive manufacturing of Co–Cr alloys for biomedical applications: A concise review,” *Journal of Materials Research*, vol. 36, no. 19. Springer Nature, pp. 3746–3760, Oct. 14, 2021. doi: 10.1557/s43578-021-00244-z.

[10] I. D. Harris, “Additive Manufacturing: A Transformational Advanced Manufacturing Technology,” *AM&P Technical Articles*, vol. 170, no. 5, pp. 25–29, May 2012, doi: 10.31399/asm.amp.2012-05.p025.

[11] A. Takaichi *et al.*, “Microstructures and mechanical properties of Co-29Cr-6Mo alloy fabricated by selective laser melting process for dental applications,” *J Mech Behav Biomed Mater*, vol. 21, pp. 67–76, May 2013, doi: 10.1016/j.jmbbm.2013.01.021.

[12] S. Eshkabilov, I. Ara, and F. Azarmi, “A comprehensive investigation on application of machine learning for optimization of process parameters of laser powder bed fusion-processed 316L stainless steel,” *International Journal of Advanced Manufacturing Technology*, vol. 123, no. 7–8, pp. 2733–2756, Dec. 2022, doi: 10.1007/s00170-022-10331-y.

[13] F. Arias-González *et al.*, “In-situ laser directed energy deposition of biomedical ti-nb and ti-zr-nb alloys from elemental powders,” *Metals (Basel)*, vol. 11, no. 8, Aug. 2021, doi: 10.3390/met11081205.

[14] N. Shahrubudin, T. C. Lee, and R. Ramlan, “An overview on 3D printing technology: Technological, materials, and applications,” in *Procedia Manufacturing*, Elsevier B.V., 2019, pp. 1286–1296. doi: 10.1016/j.promfg.2019.06.089.

[15] ASTM International, “ASTM F3187: Standard Guide for Directed Energy Deposition of Metals,” 2016, doi: 10.1520/F3187-16.

[16] D. Svetlizky, B. Zheng, D. M. Steinberg, J. M. Schoenung, E. J. Lavernia, and N. Eliaz, “The influence of laser directed energy deposition (DED) processing parameters for Al5083 studied by central composite design,” *Journal of Materials Research and Technology*, vol. 17, pp. 3157–3171, Mar. 2022, doi: 10.1016/j.jmrt.2022.02.042.

[17] A. D. Lantada, *Handbook of Active Materials for Medical Devices Advances and Applications*. Singapore: Pan Stanford Publishing Pte. Ltd., 2012.

[18] R. Saravanan, R. Hamidon, N. M. Murad, and Z. A. Zailani, “Machining of Cobalt Chromium Molybdenum (CoCrMo) Alloys: A Review,” in *Intelligent Manufacturing and Mechatronics*, 2021, pp. 413–424. doi: 10.1007/978-981-16-0866-7_36.

[19] M. Liu and M. Kuttolamadom, “Characterization of Co-Cr-Mo Alloys Manufacturing via Directed Energy Deposition,” in *International Manufacturing Science and Engineering Conference*, American Society of Mechanical Engineers, Jun. 2021. doi: 10.1115/MSEC2021-64111.

[20] A. Chiba, K. Kumagai, N. Nomura, and S. Miyakawa, “Pin-on-disk wear behavior in a like-on-like configuration in a biological environment of high carbon cast and low carbon forged Co-29Cr-6Mo alloys,” *Acta Mater*, vol. 55, no. 4, pp. 1309–1318, Feb. 2007, doi: 10.1016/j.actamat.2006.10.005.

[21] T. Odaira *et al.*, “Flexible and Tough Superelastic Co–Cr Alloys for Biomedical Applications,” *Advanced Materials*, vol. 34, no. 27, Jul. 2022, doi: 10.1002/adma.202202305.

[22] H. A. Zaman, S. Sharif, D. W. Kim, M. H. Idris, M. A. Suhaimi, and Z. Tumurkhuyag, “Machinability of Cobalt-based and Cobalt Chromium Molybdenum Alloys - A Review,” *Procedia Manuf*, vol. 11, pp. 563–570, 2017, doi: 10.1016/j.promfg.2017.07.150.

[23] A. Bandyopadhyay, K. D. Traxel, J. D. Avila, I. Mitra, S. Bose, and W. M. Keck, “CoCr Alloys,” 2020.

[24] J. H. Hong and F. Y. Yeoh, “Mechanical properties and corrosion resistance of cobalt-chrome alloy fabricated using additive manufacturing,” in *Materials Today: Proceedings*, Elsevier Ltd, 2019, pp. 196–201. doi: 10.1016/j.matpr.2020.05.543.

[25] L. Tonelli, A. Fortunato, and L. Ceschini, “CoCr alloy processed by Selective Laser Melting (SLM): effect of Laser Energy Density on microstructure, surface morphology, and hardness,” *J Manuf Process*, vol. 52, pp. 106–119, Apr. 2020, doi: 10.1016/j.jmapro.2020.01.052.

[26] B. Vandenbroucke and J. Kruth, “Selective laser melting of biocompatible metals for rapid manufacturing of medical parts,” *Rapid Prototyp J*, vol. 13, no. 4, pp. 196–203, Aug. 2007, doi: 10.1108/13552540710776142.

[27] V. D. Sartika *et al.*, “Joining dissimilar metal of Ti and CoCrMo using directed energy deposition,” *J Mater Sci Technol*, vol. 111, pp. 99–110, Jun. 2022, doi: 10.1016/j.jmst.2021.09.038.

[28] Y. Yang, C. Zhang, D. Wang, L. Nie, D. Wellmann, and Y. Tian, “Additive manufacturing of WC-Co hardmetals: a review,” *International Journal of Advanced Manufacturing Technology*, vol. 108, no. 5–6, pp. 1653–1673, May 2020, doi: 10.1007/s00170-020-05389-5.

[29] J. He and J. M. Schoenung, “A review on nanostructured WC-Co coatings,” 2002.

[30] K. W. Kim, G. S. Ham, S. H. Park, J. W. Cho, and K. A. Lee, “Direct energy deposition of ultrastrong WC-12Co cemented carbide: Fabrication, microstructure and compressive properties,” *Int J Refract Metals Hard Mater*, vol. 99, Sep. 2021, doi: 10.1016/j.ijrmhm.2021.105591.

[31] ASTM International, “ASTM F3122: Standard Guide for Evaluating Mechanical Properties of Metal Materials Made via Additive Manufacturing Processes 1,” 2014, doi: 10.1520/F3122-14.

[32] A. Sola *et al.*, “Open challenges in tensile testing of additively manufactured polymers: A literature survey and a case study in fused filament fabrication,” *Polymer Testing*, vol. 117. Elsevier Ltd, Jan. 01, 2023. doi: 10.1016/j.polymertesting.2022.107859.

[33] ASTM International, “ASTM E92: Standard Test Methods for Vickers Hardness and Knoop Hardness of Metallic Materials,” 2017, doi: 10.1520/E0092-17.

[34] M. A. Todd, J. Hunt, and I. Todd, “Investigation into using resonant frequency measurements to predict the mechanical properties of Ti-6Al-4V manufactured by selective laser melting,” *Sci Rep*, vol. 9, no. 1, Dec. 2019, doi: 10.1038/s41598-019-45696-w.

[35] F. Azarmi and I. Sevostianov, “Comparative micromechanical analysis of alloy 625 coatings deposited by air plasma spraying, wire arc spraying, and cold spraying technologies,” *Mechanics of Materials*, vol. 144, May 2020, doi: 10.1016/j.mechmat.2020.103345.

[36] ASTM International, “ASTM E1876: Standard Test Method for Dynamic Young’s Modulus, Shear Modulus, and Poisson’s Ratio by Impulse Excitation of Vibration,” 2001.

[37] A. Saboori *et al.*, “An investigation on the effect of powder recycling on the microstructure and mechanical properties of AISI 316L produced by Directed Energy Deposition,” *Materials Science and Engineering: A*, vol. 766, Oct. 2019, doi: 10.1016/j.msea.2019.138360.

[38] I. Ara, F. Azarmi, and X. W. Tangpong, “Microstructure Analysis of High-Density 316L Stainless Steel Manufactured by Selective Laser Melting Process,” *Metallography, Microstructure, and Analysis*, vol. 10, no. 6, pp. 754–767, Dec. 2021, doi: 10.1007/s13632-021-00798-8.

[39] K. F. Wang, X. H. Yang, K. C. Chou, and G. H. Zhang, “A facile route to prepare ODS WC[sbnd]Co cemented carbides,” *Int J Refract Metals Hard Mater*, vol. 98, Aug. 2021, doi: 10.1016/j.ijrmhm.2021.105569.

[40] R. N. Elshaer, A. M. Elshazli, A. H. A. Hussein, and S. R. Al-Sayed, “Impact of laser process parameters in direct energy deposition on microstructure, layer characteristics, and microhardness of TC21 alloy,” *International Journal of Advanced Manufacturing Technology*, vol. 121, no. 7–8, pp. 5139–5154, Aug. 2022, doi: 10.1007/s00170-022-09644-9.

[41] F. Azarmi, T. Coyle, and J. Mostaghimi, “Young’s modulus measurement and study of the relationship between mechanical properties and microstructure of air plasma sprayed alloy 625,” *Surf Coat Technol*, vol. 203, no. 8, pp. 1045–1054, Jan. 2009, doi: 10.1016/j.surfcoat.2008.09.035.

[42] Z. Hashin, “The Elastic Moduli of Heterogeneous Materials,” *J Appl Mech*, vol. 29, no. 1, pp. 143–150, 1962, [Online]. Available: http://asmedigitalcollection.asme.org/appliedmechanics/article-pdf/29/1/143/5444378/143_1.pdf

[43] Y. S. Al Jabbari, “Physico-mechanical properties and prosthodontic applications of Co-Cr dental alloys: A review of the literature,” *Journal of Advanced Prosthodontics*, vol. 6, no. 2, pp. 138–145, 2014, doi: 10.4047/jap.2014.6.2.138.

[44] AZoMaterials, “An Introduction to Cobalt.” Accessed: Dec. 09, 2023. [Online]. Available: https://www.azom.com/article.aspx?ArticleID=596

[45] Y. Taga, K. Kawai, and T. Nokubi, “New method for divesting cobalt-chromium alloy castings: Sandblasting with a mixed abrasive powder,” *J Prosthet Dent*, vol. 85, no. 4, pp. 357–362, 2001.

[46] A. Feldmann *et al.*, “Effect of a vinegar-hydrogen peroxide mixture on the surface properties of a cobalt-chromium alloy: A possible disinfectant for removable partial dentures,” *J Prosthet Dent*, vol. 127, no. 6, pp. 929–935, 2022.

[47] Y. Shi *et al.*, “Metal materials for Additive Manufacturing,” in *Materials for Additive Manufacturing*, First., San Diego: Academic Press, 2021, pp. 403–595.

[48] K. C. Yung, T. Y. Xiao, H. S. Choy, W. J. Wang, and Z. X. Cai, “Laser polishing of additive manufactured CoCr alloy components with complex surface geometry,” *J Mater Process Technol*, vol. 262, pp. 53–64, Dec. 2018, doi: 10.1016/j.jmatprotec.2018.06.019.

[49] L. A. Hanner, J. J. Pittari, and J. J. Swab, “Dynamic hardness of cemented tungsten carbides,” *Int J Refract Metals Hard Mater*, vol. 75, pp. 294–298, Sep. 2018, doi: 10.1016/j.ijrmhm.2018.05.007.

[50] S. F. Wayne, J. G. Baldoni, and S. T. Buljan, “Abrasion and Erosion of WC-Co with Controlled Microstructures,” *Tribology Transactoins*, vol. 33, no. 4, pp. 611–617, 1990.

[51] D. B. Marshall, T. Noma, and A. G. Evans, “A Simple Method for Determining Elastic-Modulus–to-Hardness Ratios using Knoop Indentation Measurements,” *Journal of the American Ceramic Society*, vol. 65, no. 10, Oct. 1982, doi: 10.1111/j.1151-2916.1982.tb10357.x.

[52] N. Meredith, M. Sherriff,’, D. J. Setchell, and S. A. V Swanson, “Measurement of the Microhardness and Young’s Modulus of Human Enamel and Dentine Using an Indentation Technique,” 1996.

[53] V. V. Ganesh and N. Chawla, “Effect of particle orientation anisotropy on the tensile behavior of metal matrix composites: Experiments and microstructure-based simulation,” *Materials Science and Engineering: A*, vol. 391, no. 1–2, pp. 342–353, Jan. 2005, doi: 10.1016/j.msea.2004.09.017.

[54] J. Wilson, “Metallic biomaterials,” in *Fundamental Biomaterials: Metals*, Elsevier, 2018, pp. 1–33. doi: 10.1016/B978-0-08-102205-4.00001-5.

[55] B. V. Krishna, S. Bose, and A. Bandyopadhyay, “Low stiffness porous Ti structures for load-bearing implants,” *Acta Biomater*, vol. 3, no. 6, pp. 997–1006, 2007, doi: 10.1016/j.actbio.2007.03.008.

[56] K. B. Hazlehurst, C. J. Wang, and M. Stanford, “An investigation into the flexural characteristics of functionally graded cobalt chrome femoral stems manufactured using selective laser melting,” *Mater Des*, vol. 60, pp. 177–183, 2014, doi: 10.1016/j.matdes.2014.03.068.

[57] P. A. Kobryn and S. L. Semiatin, “Mechanical Properties of Laser-Deposited Ti-6Al-4V,” 2001.

[58] S. Dongare, T. E. Sparks, J. Newkirk, and F. Liou, “A Mechanical Testing Methodology for Metal Additive Manufacturing Processes Manufacturing Engineering + Mechanical Engineering,” 2014.

[59] M. F. Slim, A. Alhussein, A. Billard, F. Sanchette, and M. François, “On the determination of Young’s modulus of thin films with impulse excitation technique,” *J Mater Res,* vol. 32, no. 3, pp. 497–511, Feb. 2017, doi: 10.1557/jmr.2016.442.

[60] J. Tomas, T. Schubert, T. Bernthaler, M. Merkel, G. Schneider, and D. Sellmer, “Laser sintering of tungsten carbide cutter shafts with intergrated cooling channels,” in *Proceedings of the International Conference on Progress in Additive Manufacturing*, Pro-AM, 2018, pp. 297–302. doi: 10.25341/D48G6C.

[61] Y. Y. Santana *et al.*, “Influence of mechanical properties of tungsten carbide-cobalt thermal spray coatings on their solid particle erosion behaviour,” *Surface Engineering*, vol. 28, no. 4, pp. 237–243, May 2012, doi: 10.1179/1743294411Y.0000000016.

[62] P. Chivavibul, M. Watanabe, S. Kuroda, and K. Shinoda, “Effects of carbide size and Co content on the microstructure and mechanical properties of HVOF-sprayed WC-Co coatings,” *Surf Coat Technol*, vol. 202, no. 3, pp. 509–521, Dec. 2007, doi: 10.1016/j.surfcoat.2007.06.026.

APPENDIX A. MATLAB CODE

A.1. Newton Raphson Method of Pautrot Model for Resonance Frequency Analysis of Coated Section

```
% Clearing Screen
clear
clc
format long

%Constants
b=6.28E-6;
ht=7.21E-6;
hs=6.43E-6;
hc=ht-hs;
Et=199.91E9;
Es=215.93E9;
It=(1/12)*b*(ht^3);

%Newton Raphson Method
k=0;
Ec=200E9;
fx=inf;
while abs(fx)>1E-100
    k=k+1;
    e=(((Es*(hs^2))-(Ec*(hc^2)))/(2*Es*hs+2*Ec*hc));

    Is=(1/12)*b*(hs^3)+b*hs*(((hs/2)-e)^2);

    Ic=(1/12)*b*(hc^3)+b*hc*(((hc/2)+e)^2);

    fx=Es*Is+Ec*Ic-Et*It;
    dfx=(b*hc^3)/12 + b*hc*(hc/2 - (Ec*hc^2 - Es*hs^2)/(2*Ec*hc + 2*Es*hs))^2
- 2*Ec*b*hc*(hc^2/(2*Ec*hc + 2*Es*hs) - (2*hc*(Ec*hc^2 - Es*hs^2))/(2*Ec*hc +
2*Es*hs)^2)*(hc/2 - (Ec*hc^2 - Es*hs^2)/(2*Ec*hc + 2*Es*hs)) +
2*Es*b*hs*(hc^2/(2*Ec*hc + 2*Es*hs) - (2*hc*(Ec*hc^2 - Es*hs^2))/(2*Ec*hc +
2*Es*hs)^2)*(hs/2 + (Ec*hc^2 - Es*hs^2)/(2*Ec*hc + 2*Es*hs));

    Ec=Ec-(fx/dfx);
    values(k,1)=k;
    values(k,2)=Ec;
    values(k,3)=fx;
end
```

APPENDIX B. ADDITIONAL OOF SIMULATIONS

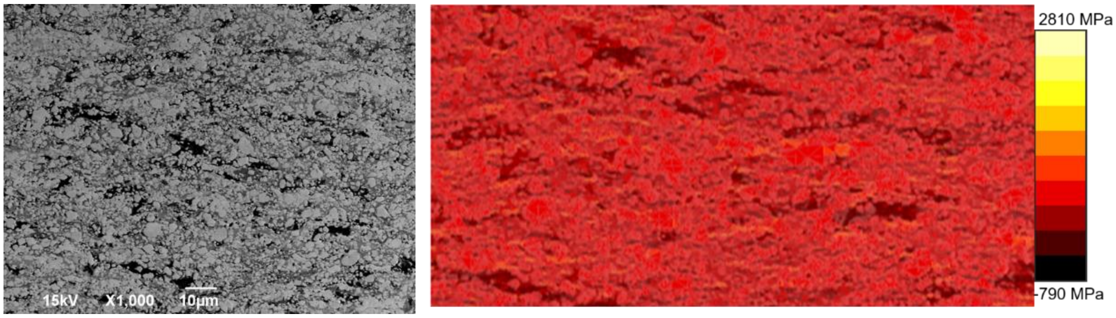

Figure B.1. HVAF WC-Co OOF Simulation at 1000x Magnification Example 2

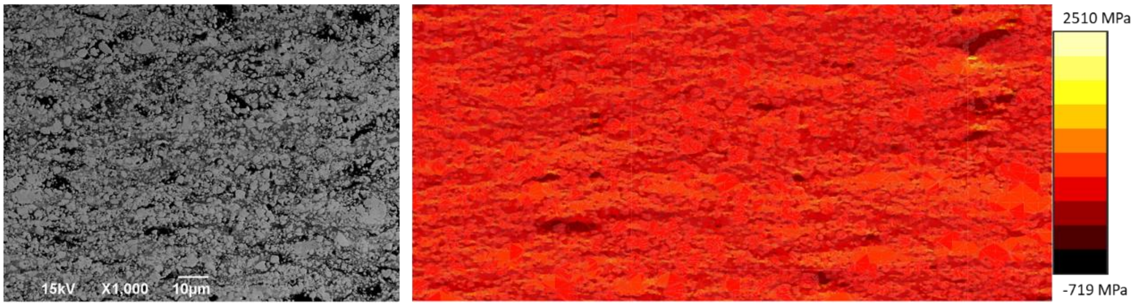

Figure B.2. HVAF WC-Co OOF Simulation at 1000x Magnification Example 3

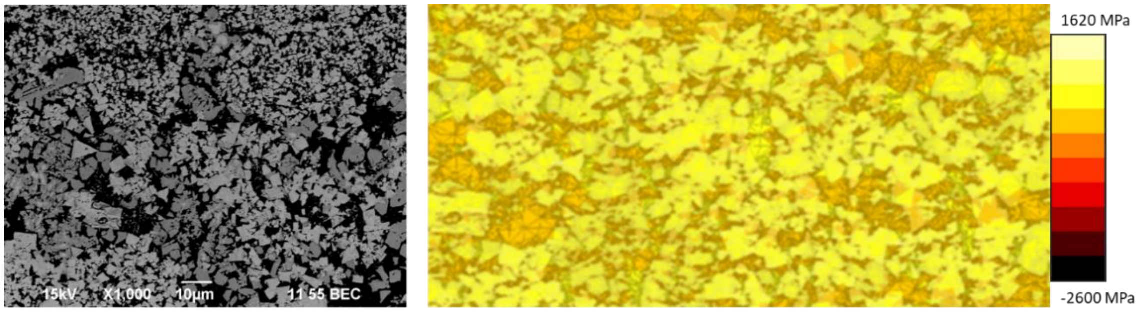

Figure B.3. DED WC-Co OOF Simulation of the Top Region at 1000x Magnification

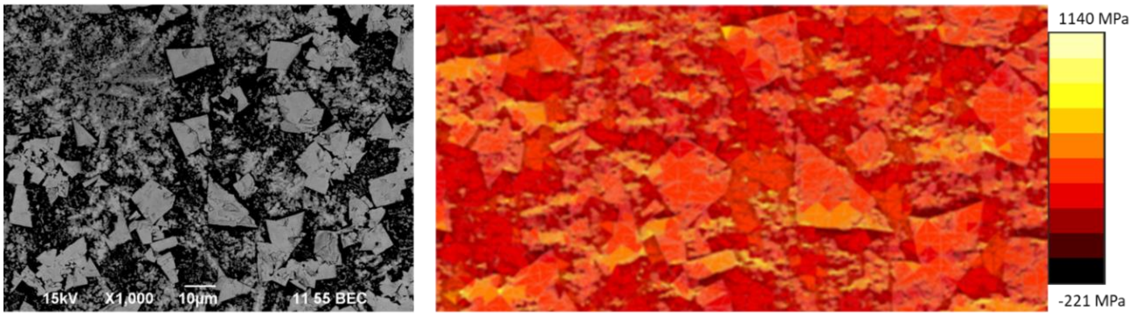

Figure B.4. DED WC-Co OOF Simulation of Middle Region at 1000x Magnification

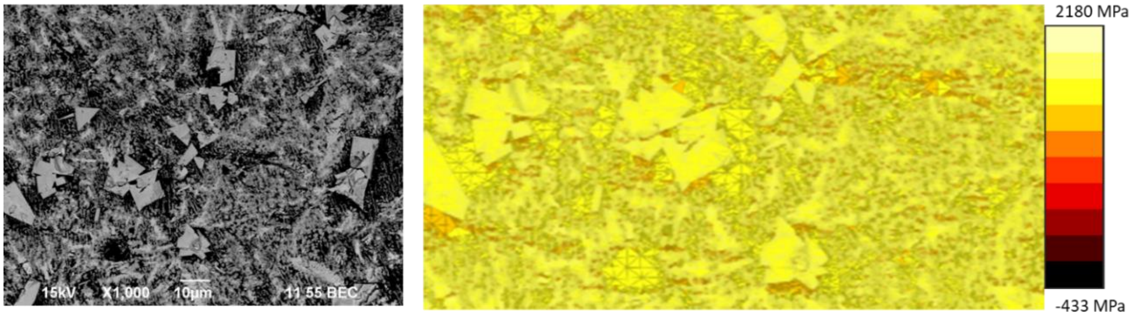

Figure B.5. DED WC-Co OOF Simulation of Bottom Region at 1000x Magnification